

**PLACE IN RETURN BOX** to remove this checkout from your record.  
**TO AVOID FINES** return on or before date due.  
**MAY BE RECALLED** with earlier due date if requested.

DATE DUE	DATE DUE	DATE DUE

**FOURIER SERIES BASED IMPLICIT FEM PROGRAM FOR AXISYMMETRIC  
ANALYSIS OF TUBE HYDROFORMING**

**By**

**Manish Sharma**

**A THESIS**

**Submitted to  
Michigan State University  
in partial fulfillment of the requirements  
for the degree of**

**MASTER OF SCIENCE**

**Department of Mechanical Engineering**

**2003**

## **ABSTRACT**

### **FOURIER SERIES BASED IMPLICIT FEM PROGRAM FOR AXISYMMETRIC ANALYSIS OF TUBE HYDROFORMING**

**By**

**Manish Sharma**

Tube Hydroforming has become a preferred alternative to stamping and joining processes in industry for manufacturing closed cross section structural components. This process requires proper combination of part design, material selection, application of internal pressure and axial feeding. By using finite element analysis, these process parameters can be determined efficiently in the very early stage of production.

The thesis presents a Fourier series based axisymmetric analysis of Tube Hydroforming. The material is assumed to elastic-plastic and to satisfy the plasticity model that takes into account rate independent work hardening and normal anisotropy. Numerical solution obtained from Total-Lagrangian formulation of general shell theory is employed. The axial stroke is incorporated using Lagrange multipliers. Contact violation and boundary friction condition are introduced into the formulation based on penalty functions, which impose constraints directly into the tangent stiffness matrix. The Force Limiting Curves based on shear instability and on experimental results are used as fracture criteria. The Axisymmetric Hydroforming program developed is verified against results from Abaqus and experimental measurements for isotropic and anisotropic (transverse) materials.

## **ACKNOWLEDGMENTS**

The author wishes to express his appreciation to the following people for making the completion of his Master of Science possible.

To my major professor, Dr. Farhang Pourboghraat, for his help, patience and guidance, without which this project would not have been possible.

To Guan Yabo for his help in extending this code and also in preparing this manuscript.

## TABLE OF CONTENTS

LIST OF FIGURES.....	vi
INTRODUCTION.....	1
CHAPTER 1	
LITERATURE REVIEW.....	4
CHAPTER 2	
THIN SHELL THEORY.....	9
Principal Stretch (Total Lagrangian).....	9
Principal Curvature and Stretch (Updated Lagrangian).....	12
CHAPTER 3	
KINEMATICS.....	16
Kinematics Assumptions.....	16
Principal Strains.....	16
Constraints.....	18
CHAPTER 4	
CONSTITUTIVE EQUATION.....	20
CHAPTER 5	
CONTACT ALGORITHM.....	22
Numerical Procedures for Contact.....	22
Detection of Contact.....	24
Contact Tolerance.....	24
Normal Vector and Tangential Vector.....	25
Condition for Contact Violation.....	27
The Projection Algorithm.....	28
The Iterative Method.....	28
The Directive Method.....	29
Implementation of Constraint.....	30
Friction Model.....	30
Separation.....	32
CHAPTER 6	
NUMERICAL SIMULATION.....	33
Principle of Virtual Work.....	33
Newton-Raphson Algorithm.....	34
Four Types of Modeling.....	35
Pressure Loading Modeling.....	35
Axial Loading Modeling.....	38

Displacement Stroke Modeling.....	38
Frictional Contact Modeling.....	39
Fracture Criteria.....	43
 <b>CHAPTER 7</b>	
PROGRAM STRUCTURE.....	45
Input File.....	45
Geometric, Numerical and Material Input.....	45
Loading Input.....	49
Program Flow Chart.....	51
Output File.....	52
 <b>CHAPTER 8</b>	
EXAMPLES.....	54
Aluminium Tube Example.....	54
Steel Tube Example.....	57
 <b>CHAPTER 9</b>	
CONCLUSIONS.....	73
 APPENDIX A.....	 75
APPENDIX B.....	77
REFERENCES.....	80

## LIST OF FIGURES

Figure 0.1 Representative hydroformed components and assemblies.....	2
Figure 0.2 Principal hydroforming tooling diagram.....	2
Figure 1.1 Hydroforming Process Sequence.....	6
Figure 2.1 Shell element at original time $t_0$ and current time $t$ (Total Lagrangian).....	11
Figure 2.2 Shell mid-surface at reference time $^0t$ and current time $t$ (Total Lagrangian).....	11
Figure 3.1 Representative Meridian for axisymmetric case.....	16
Figure 3.2 Geometry of a straight segment.....	17
Figure 5.1 Contact tolerance.....	25
Figure 5.2(a) The computational mesh (b) The normal vector and tangent vector.....	26
Figure 5.3 The associated die segment with contact node.....	28
Figure 5.4 The projection algorithm.....	29
Figure 5.5 Coulomb friction model.....	31
Figure 6.1 A schematic of tool-workpiece check.....	40
Figure 6.2 Flow chart for contact iteration.....	42
Figure 7.1 Flow chart of the program.....	51
Figure 8.1 Current Radius vs. Tube Length .....	60
Figure 8.2 Hoop Strain vs. Tube Length (Aluminium).....	61
Figure 8.3 Axial Strain vs. Tube Length (Aluminium).....	62
Figure 8.4 Thickness vs. Pressure.....	63

Figure 8.5 Hoop strain distribution compared with Abaqus.....	64
Figure 8.6 Axial strain distribution compared with Abaqus.....	65
Figure 8.7 Hoop strain comparison for different yield functions and Experimental Measurements.....	66
Figure 8.8 Current Radius vs. Tube Length.....	67
Figure 8.9 Displacement Stroke vs. Internal Pressure History.....	68
Figure 8.10 Hoop Strain vs. Tube Length (Steel).....	69
Figure 8.11 Axial Strain vs. Tube Length (Steel).....	70
Figure 8.12 Thickness vs. Pressure at maximum bulge point.....	71
Figure 8.13 Major vs. Minor Strain.....	72



## **INTRODUCTION**

Hydroforming offers a way to cut material and manufacturing costs while improving product performance in a variety of applications. Advantages include weight reduction due to improved part design, part consolidation where a single component replaces an assembly, reduced tooling cost as a result of part consolidation, and improved structural strength and stiffness of the hydroformed component. It thus reduces tooling, part, and labor costs, while significantly improving product performance (Anon, 1997).

The process currently is being used or being considered for making a wide range of complex cylindrical, flat and tubular components. Cylindrical parts include gas cylinders, washing-machine drums, and cooker cavities. Flat components include auto body panels, fuel tanks, and aerospace parts.

Tube hydroforming is receiving the greatest attention, especially in the auto industry (Vari-Form Inc, 1998), because existing multi-piece, stamped/welded assemblies in auto body and frame structures potentially can be replaced with less expensive hydroformed parts that are lighter, stronger and more precise (Figure 0.1).

In tube hydroforming, internal pressure is applied to form a tubular metal blank into a structural component having a closed cross section. As shown in Figure 0.2, a straight or prebent tube is placed in an open die, the die is closed, the tube ends are sealed, and the tube is filled with a hydraulic fluid. Internal hydraulic pressure forces the tube to conform to the shape of the die cavities, producing a part having different cross-section shapes.



Figure 0.1 — Representative hydroformed components and assemblies  
 From left to right: instrument panel support beam, engine-cradle assembly.  
 Photo courtesy Vari-Form, Woodstock, Ontario, Canada.

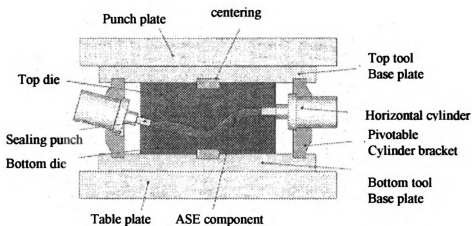


Figure 0.2 — Principal hydroforming tooling diagram  
 Courtesy Schafer Hydroforming, Wilsdorf, Germany.

The thesis presents an axisymmetric analysis method for calculating strains and expansion as the tube is subject to simultaneous internal pressure and axial displacement stroke. Only free forming stage of tube hydroforming is treated.

The present method employs a number of simplifying assumptions. The principal geometrical assumption is that the representative meridian of the tube is initially straight. All segments making up the meridian are assumed to be relatively thin and of constant thickness. The deformation of the member is assumed not to vary along the cross-section of the tube. Hence, the analysis can be considered to be an axisymmetric analysis.

The material is assumed to be elastic-plastic and to satisfy the plasticity model that takes into account rate-independent, work hardening and normal anisotropy (Pourboghrat et al, 2000).

At the tool-tube interface, the frictional stress is assumed, on the basis of ordinary Coulomb friction, to be proportional to the contact pressure whenever relative sliding occurs.

By using the virtual work principle and constitutive equation, the equilibrium equation can be derived. Numerical solution obtained from a Total-Lagrangian formulation of a general shell theory is employed. Axial stroke is incorporated into the equilibrium equation using Lagrange Multiplier technique. The boundary friction condition is introduced into the formulation in the form of penalty function, which imposes the constraints directly into the tangent stiffness matrix. The Newton-Raphson algorithm is used to solve the nonlinear equation. Force Limiting Curve equations based on the onset of shear instability and on experimental measurements are incorporated as the fracture criteria.

# **CHAPTER 1**

## **LITERATURE REVIEW**

### **1.1 Hydroforming Concept**

Hydroforming has been one of the fundamental sheet metal forming processes for quite a long time, having been developed at least since pre-World War II, when it was applied to the German aircraft industry (Zhang, 1997). About 30 years ago, the first hydroformed parts were fabricated by expanding a straight or prebent tube to make manifold elements and components of similar geometry for sanitary use. Today, many hydroformed parts are already in mass-production in the automotive industry. Well-known hydroformed automotive applications include exhaust manifolds, exhaust pipes and subframes, such as radiator enclosures, space frames, dash assemblies, frame rail, engine cradles, etc. (Dohman et al, 1997)

According to its features, hydroforming can be classified as the following processes (Zhang, 1999 and Siegert et al, 2000):

1. Flat sheet hydroforming or hydroforming deep drawing
2. Tube hydroforming or hydrobulging of tubular components
3. Hydromechanical deep drawing process
4. New variation of hydroforming including the integral hydrobulge forming (IHBF) of sheet shell products and viscous pressure forming (VPF) processes

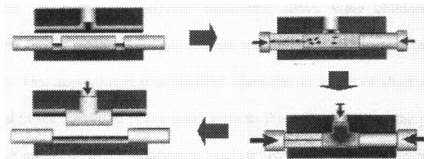
In this thesis, we focus on tube hydroforming that has become an economic alternative to various stamping processes with the availability of advanced machine design and controls.

Tube hydroforming offers several advantages as compared to conventional manufacturing via stamping and welding (Ahmetoglu et al, 2000). These include:

- (a) part consolidation (stamped and resistance welded two or more pieces of a box section can be manufactured in one operation from a hollow component)
- (b) weight reduction through more efficient section design and tailoring of the wall thickness
- (c) improved structural strength and stiffness
- (d) lower tooling cost due to fewer parts
- (e) fewer secondary operation (no welding of sections required and holes may be punched during hydroforming)
- (f) tight dimensional tolerances and low springback
- (g) reduced scrap

While numerous variations of hydroforming exist, the basic principle remains the same: utilize fluid pressure to form a component. Both traditional high-pressure hydroforming and pressure sequence hydroforming are presented in Longhouse (1998) and Morphy (1997). Typical Hydroforming sequence is shown below (Fig. 1.1), where internal pressure and axial feed are applied simultaneously to improve the material shaping abilities.

- 1) Place the blank tube into tooling
- 2) Seal the ends and fill with fluid



- 4) Open the tooling, remove the part
- 3) Increase pressure, move punches

Fig. 1.1 Hydroforming process sequence (Leitloff, F. 1997)

If hydroforming technology is to be applied economically, it is essential to have knowledge of the avoidance of failure cases as well as of the behavior of the tube in the tool under the compressive stress and forces that are exerted by the machine (i.e., axial feed). Several failure modes, buckling, wrinkling and bursting are shown in Dohmann (1996) and Asnafi (1999).

## 1.2 Numerical Simulation

Kobayashi (1989) has worked on several sheet forming problems including drawing, bulging, stretch forming and bending, solving the problems using a finite element method based on incremental strain theory. In his work, the material was assumed as rigid-plastic and anisotropy and work hardening characteristics were

included. An elastic-plastic FEM formulation of stretch forming for a punch and a die of arbitrary shape was introduced by Wang and Bundiansky (1978), which is a classic example verified by ABAQUS. A rigid-viscoplastic material model FEM formulation was presented by Germain, Chung and Wagoner (1989).

All the numerical analyses mentioned above were obtained using simple membrane theory which does not include the variation of stresses through the sheet thickness. This approximation is justified when the thickness of sheet material is small compared to the curvature of the sheet surface, the radius of either the punch or the die, and when in-plane stretch dominates bending. However, in order to simulate bending phenomena such as the early deformation in stretch forming, spring-back etc., inclusion of the bending stress is necessary. A total Lagrangian formulation based on an extension of a thin shell theory which takes into account large membrane and bending strain was derived by Wang and Tang (1988). An updated Lagrangian and plane-strain bending formulation based on nonlinear thin-shell theory was employed by Choudhry and Lee (1994). A general purpose finite element program for analysis of forming processes, which was implemented in MARC, was introduced by Nagtegaal and Rebelo (1988).

Built on the successful application of finite element method on sheet metal forming, explicit finite element method is being applied to hydroforming of tubular parts by Ni (1994), bulging process by Hu et al. (1997), and a sheet metal operation involving punch stretching, drawing and hydroforming by Hsu and Chu (1995). In Noh and Yang (1998) work, a general formulation for hydroforming of arbitrarily shaped boxes was expressed.

### **1.3 Friction and Contact Problem**

Friction and contact between sheet and die play an important role in hydroforming processes. Classical Coulomb's law is capable of describing only friction effects between effectively rigid bodies and gross sliding of one body relative to another, However if Coulomb's law is applied pointwise in contact problem, then the contact stress developed normal to the contact surface is ill defined. In Oden and Pires (1983), nonlocal and nonlinear friction laws and variational principles for contact problems were introduced.

A method of discretizing the die boundary condition considered for the analysis of metal forming processes with arbitrary shaped dies was employed by Oh (1982).



## CHAPTER 2

### THIN SHELL THEORY

The deformation of the mid-surface of an element in the plane containing the meridian curve will be considered. The deformation of the element will be obtained from the theory of thin shells and Figure 2.1-2.2 show the mid-surface of an element of the sheet at the initial time  $t_0$ , reference time  ${}^0t$  and at the current time  $t$  as it bends and stretches. Derivation of principal curvatures and stretches of a shell element undergoing an axisymmetric deformation was discussed in (Pourboghraat, F. et al, 2000) using both total and updated Lagrangian formulations. These formulations are used in the program.

#### 2.1 Principal Stretch (Total Lagrangian Formulation)

Figure 2.1 shows a flat element at the initial time  $t_0$  and at the current time  $t(={}^0t+\Delta t)$  as it bends and stretches. By referring to Figure 2.1, the following relationship between the current and the initial position vectors and the total displacement vector for the mid-surface of the element can be written:

$$\underset{\sim}{x} = \underset{\sim}{X} + \underset{\sim}{U} \quad (2.1)$$

where the initial position vector  $\underset{\sim}{X}$  and the total displacement vector  $\underset{\sim}{U}$  are, defined in the global coordinate system,

$$\underset{\sim}{X} = \begin{bmatrix} X_1 \\ 0 \end{bmatrix}, \quad \underset{\sim}{U} = \begin{bmatrix} u \\ w \end{bmatrix} \quad (2.2)$$

In Eq.(2.2),  $u$  and  $w$  are the total displacements of the mid-surface. By substituting from Eq.(2.2) into (2.1), the position vector  $\underset{\sim}{x}$  becomes

$$\underset{\sim}{x} = \begin{bmatrix} X_1 + u \\ w \end{bmatrix} \quad (2.3)$$

To calculate the principal stretch in the radial direction, we will consider the unit tangent vector,  $\hat{\underline{a}}$ , of the current mid-surface, i.e.

$$\hat{\underline{a}} = \frac{d\underline{x}}{ds} = \frac{d\underline{x}}{dS} \frac{dS}{ds} = \frac{d\underline{x}}{dX_1} \frac{1}{\lambda_1^0} = \begin{bmatrix} 1 + u_{,X_1} \\ w_{,X_1} \end{bmatrix} \frac{1}{\lambda_1^0} \quad (2.4)$$

where  $\lambda_1^0 = ds/dS$ . Here,  $s$  and  $S$  are travel length of the current and initial surfaces from center, respectively, and the comma stands for the differentiation with respect to  $X_1$ . Then, by calculating the magnitude of vector  $\hat{\underline{a}}$  from Eq.(2.4) and setting it equal to unity,  $\lambda_1^0$  can be calculated to be:

$$\|\hat{\underline{a}}\| = \sqrt{\hat{\underline{a}} \cdot \hat{\underline{a}}} = 1.0 \quad (2.5)$$

$$\lambda_1^0 = [(1 + u_{,X_1})^2 + w_{,X_1}^2]^{1/2} \quad (2.6)$$

The principal stretch in the circumferential direction,  $\lambda_2^0$ , is calculated from the change in the radial position of the element; i.e.

$$\lambda_2^0 = \left[ \left( \frac{X_1 + u}{X_1} \right) \right] = 1 + \frac{u}{X_1} \quad (2.7)$$

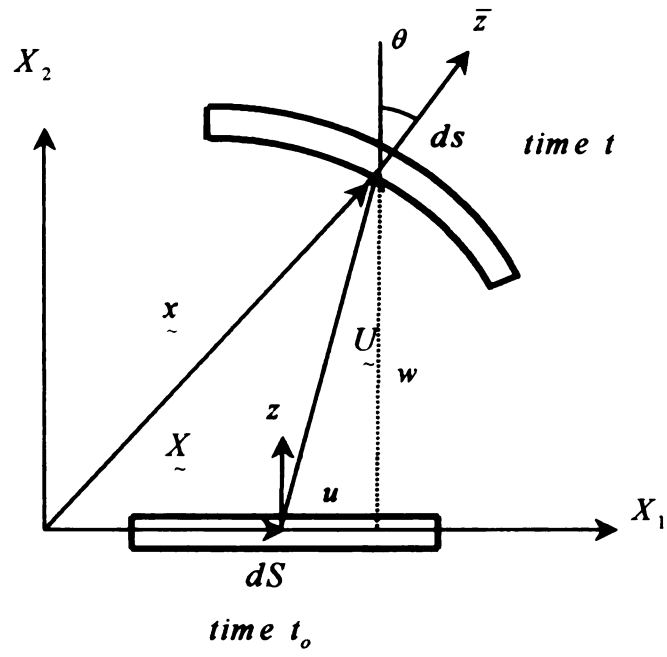


Figure 2.1 Shell element at original time  $t_0$  and current time  $t$ (Total Lagrangian)

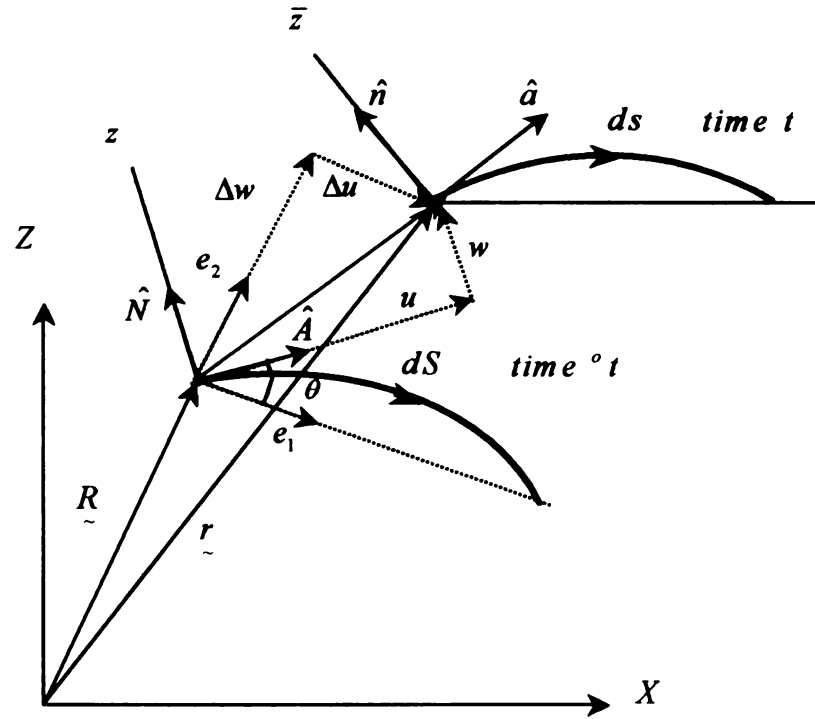


Figure 2.2 Shell mid-surface at reference time  ${}^\circ t$  and current time  $t$ (Updated Lagrangian)

## 2.2 Principal Curvature and Stretch (Updated Lagrangian)

After bending and stretching, the principal mid-surface curvature,  $k_1$ , of a shell element at the current configuration,  $t(=^0t+\Delta t)$ , can be calculated from the known information about the element at the reference configuration (time  $^0t$ , see Figure 2.2), as follows:

$$\underline{\underline{r}} = \underline{\underline{R}} + u \underline{\underline{\hat{A}}} + w \underline{\underline{\hat{N}}} \quad (2.8)$$

where  $\underline{\underline{R}}$  is the reference configuration at time  $^0\tau$  and  $u$  and  $w$  are incremental displacements defined in Figure 2.2. In Eq.(2.8), the unit tangent vector  $\underline{\underline{\hat{A}}}$  and the unit principal normal vector  $\underline{\underline{\hat{N}}}$  to the mid-surface of the reference are defined as

$$\underline{\underline{\hat{A}}} = \frac{\partial \underline{\underline{R}}}{\partial S} = \underline{\underline{R}}_{,s} \quad (2.9)$$

$$\underline{\underline{\hat{N}}} = \frac{\underline{\underline{\hat{A}}}_{,s}}{K_1} \quad (2.10)$$

where  $K_1$  is the curvature. Therefore,

$$\underline{\underline{\hat{N}}} \cdot \underline{\underline{\hat{A}}} = 0 \quad (2.11)$$

and

$$-K_1 \underline{\underline{\hat{A}}} = \underline{\underline{\hat{N}}}_{,s} \quad (2.12)$$

To calculate the current curvature,  $k_1$ , the unit tangent vector  $\hat{\underline{a}} = \frac{\underline{a}}{\|\underline{a}\|}$  and the

unit principal normal vector of the mid-surface of the shell  $\hat{\underline{n}} = \frac{\underline{n}}{\|\underline{n}\|}$  are calculated.

Using Eq.(2.8), the tangent vector  $\underline{a}$  is found as:

$$\underline{a} = \frac{\partial \underline{r}}{\partial S} = \underline{r}_{,s} = \underline{R}_{,s} + \underline{u}_{,s} \hat{\underline{A}} + \underline{u} \hat{\underline{A}}_{,s} + \underline{w}_{,s} \hat{\underline{N}} + \underline{w} \hat{\underline{N}}_{,s} \quad (2.13)$$

By substituting from Eqs.(2.9), (2.10) and (2.12) into (2.13), and re-arranging, the following expression results:

$$\underline{a} = \frac{\partial \underline{r}}{\partial S} = \underline{r}_{,s} = (1 + \underline{u}_{,s} - K_1 \underline{w}) \hat{\underline{A}} + (\underline{w}_{,s} + K_1 \underline{u}) \hat{\underline{N}} = c \hat{\underline{A}} + d \hat{\underline{N}} \quad (2.14)$$

The principal incremental stretch of the mid-surface in the radial direction calculated from the magnitude of the base vector  $\underline{a}$  in Eq.(2.14) is

$$\lambda_1 = \|\underline{a}\| = \sqrt{\underline{a} \cdot \underline{a}} = \sqrt{c^2 + d^2} = [(1 + \underline{u}_{,s} - K_1 \underline{w})^2 + (\underline{w}_{,s} + K_1 \underline{u})^2]^{\frac{1}{2}} \quad (2.15)$$

The current length of the mid-surface of the shell in the radial direction,  $ds$ , is calculated from the reference length,  $dS$ , and  $\lambda_1$  as follows:

$$ds = \lambda_1 dS \quad (2.16)$$

The unit principal normal vector of the surface of the current shell,  $\hat{\underline{n}}$ , is

$$\hat{\underline{n}} = \frac{-d \hat{\underline{A}} + c \hat{\underline{N}}}{\lambda_1} \quad (2.17)$$

which, from Eqs.(2.14), (2.15) and (2.17), shows that  $\hat{n} \cdot \hat{a} = 0$ . The current principal curvature of the shell,  $k_1$ , can now be found as:

$$k_1 = -\hat{a} \cdot \hat{n} = -\mathbf{r} \cdot \hat{n} = -\frac{1}{\lambda_1^2} \mathbf{a} \cdot \hat{n} \quad (2.18)$$

where  $\mathbf{a}$  is given by Eq.(2.13) and  $\hat{n}$  can be derived from Eq.(2.17):

$$\hat{n} = \frac{d\hat{n}}{dS} = \frac{\lambda_1 \cdot (d_{,s} \hat{A} + c_{,s} \hat{N} - K_1 c \hat{A} - K_1 d \hat{N}) - \lambda_{1,s} \cdot (-d \hat{A} + c \hat{N})}{\lambda_1^2} \quad (2.19)$$

In Eq.(2.19),  $\lambda_{1,s}$  is assumed to vanish within an element and the above expression simplifies as :

$$\hat{n} = -\frac{(d_{,s} + K_1 c) \hat{A} + (-c_{,s} + K_1 d) \hat{N}}{\lambda_1} \quad (2.20)$$

By substituting from Eqs.(2.14), (2.15) and (2.20) into Eq.(2.18), the current centerline curvature of the shell,  $k_1$ , can be found:

$$k_1 = \frac{cd_{,s} - dc_{,s} + K_1 \lambda_1^2}{\lambda_1^3} \quad (2.21)$$

It should be noted that it is possible to recover Eq.(2.7), for total Lagrangian formulation, From Eq.(2.15). This is done by setting the reference curvature  $K_1$  equal to zero for a flat sheet, replacing  $S$  with  $X_1$  and treating the incremental displacement  $\mathbf{u}$  and  $\mathbf{w}$  as total displacements in Eqs.(2.14) and (2.15). Similarly, the current curvature of the shell,  $k_1$ , can be calculated from the initial configuration by setting  $K_1$  equal to zero, replacing  $\lambda_1$  with  $\lambda_1^o$  and  $S$  with  $X_1$  and treating  $\mathbf{u}$  and  $\mathbf{w}$  as total displacements in Eq.(2.21)

$$k_1 = \frac{[-\mathbf{w}_{,X_1} \mathbf{u}_{,X_1 X_1} + (1 + \mathbf{u}_{,X_1}) \mathbf{w}_{,X_1 X_1}]}{(\lambda_1^o)^3} \quad (2.22)$$

The current principal stretch increment of the mid-surface of the shell in the circumferential direction,  $\lambda_2$ , is found from the geometry (in Fig. 2.2) as:

$$\lambda_2 = \frac{r_1}{R_1} \quad (2.23)$$

The principal curvature of the shell in the circumferential direction,  $k_2$ , is found from Fig. 2.1 (Flugge, 1973), as follows:

$$k_2 = \frac{1}{r_2} = -\frac{\sin \theta}{R} = -\frac{1}{R} \frac{\partial w}{\partial s} = -\frac{w_{,s}}{R} \quad (2.24)$$

where  $w$  and  $s$  were defined previously and  $R$  is defined as (see Fig. 2.1):

$$R = X_1 + u \quad (2.25)$$

Since it is known that  $\partial s = \lambda_1^0 \partial X_1$ , Eq. (2.24) becomes

$$k_2 = -\frac{1}{R} \frac{\partial w}{\partial s} = -\frac{1}{R} \frac{\partial w}{\partial X_1} \frac{\partial X_1}{\partial s} = -\frac{1}{\lambda_1^0 R} \frac{\partial w}{\partial X_1} = -\frac{w_{,X_1}}{\lambda_1^0 R} \quad (2.26)$$

Finally, by substituting from Eq. (2.25) into Eq. (2.26), we get the following expression for the principal curvature in the circumferential direction:

$$k_2 = -\frac{w_{,X_1}}{[(X_1 + u) \lambda_1^0]} \quad (2.27)$$

## CHAPTER 3

### KINEMATICS

Based on the general thin shell formulations in Chapter 2, the formulations for finite strain and small rotation have been derived for the straight-line segment that are used in the program. (Derivation in details can be seen in Appendix A).

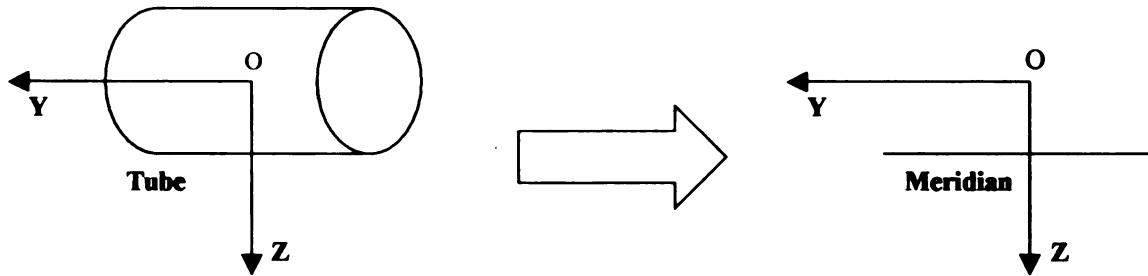


Fig 3.1 Representative Meridian for axisymmetric case

#### 3.1 Kinematics Assumptions

For the purpose of modeling, all segments making up the meridian are assumed to be thin and of constant thickness. The length of the straight segments should be greater than ten times the thickness. The deformation of the structural member is assumed not to vary along its cross-section for a given point on the meridian. Hence, the analysis can be done for a straight meridian parallel to the axis of the tube.

#### 3.2 Principal Strains

The representative meridian shown in Figure 3.1 lies in the plane defined by the  $Y$  and  $Z$ -axes. In this formulation, the initial geometry of the meridian is specified by first defining the  $Y$ - $Z$  coordinates of a set of nodes and then defining the segments. Two nodes must bind each segment.



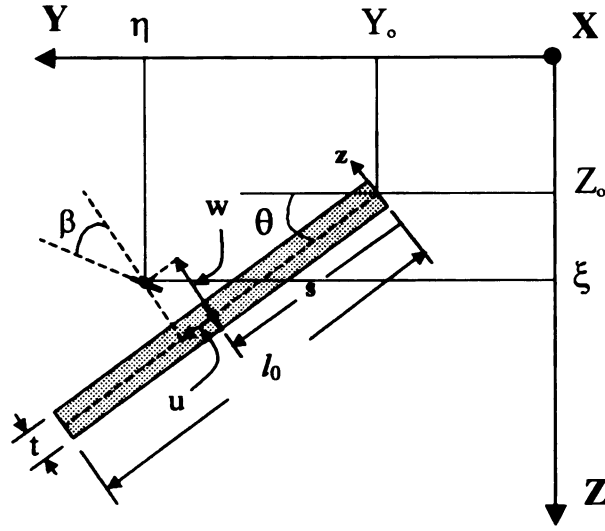


Figure3.2 Geometry of a straight segment

For the straight segment in Figure 3.2, the local coordinates of the segment are  $s$  along the segment and  $z$  in the through-thickness direction. The initial segment geometry is defined by the location of the point  $s = 0$  given by  $Y_0$  and  $Z_0$ , the orientation angle  $\theta$ , the length  $l_0$  and the thickness  $t$  of the segment. The position  $z=0$  is located at the mid-surface of the segment, indicated by the dashed line. The displacement components of the mid-surface are  $u$  and  $w$  along the original  $s$  and  $z$  directions respectively. The rotation of a line is given by  $\beta$

$$\beta = -\frac{dw}{ds} = -w_{,s} \quad (3.1)$$

The coordinates of a point on a segment undergoing displacements  $u$  and  $w$  from the original configuration are (see Fig. 3.2) :

$$\xi = Z_0 + (s + u) \sin \theta - w \cos \theta + z(-\cos \theta + \beta \sin \theta) \quad (3.2a)$$

$$\eta = Y_0 + (s + u) \cos \theta + w \sin \theta + z(\sin \theta + \beta \cos \theta) \quad (3.2b)$$

The axial strain component  $\epsilon_x$  along the length of the tube is given by

$$\epsilon_x = \epsilon_x^0 + \kappa_x z \quad (3.3)$$

where  $\epsilon_x^0$  is the membrane strain component given by

$$\epsilon_x^0 = u_{,s} + \frac{1}{2}u_{,s}^2 + \frac{1}{2}w_{,s}^2 \quad (3.4)$$

where the local curvature is given by

$$\kappa_x = \frac{w_{,ss}}{(1 + w_{,s}^2)^{\frac{3}{2}}} \quad (3.5)$$

The strain component in the circumferential direction is given by

$$\epsilon_r = \epsilon_r^0 + \kappa_r z \quad (3.6)$$

where  $\epsilon_r^0$  is given by

$$\epsilon_r^0 = \frac{\xi - (Z_0 + s \sin \theta - z \cos \theta)}{R} = \frac{u \sin \theta - w \cos \theta + z \beta \sin \theta}{R} \quad (3.7)$$

and the local curvature  $\kappa_r$  is given by

$$\kappa_r = -\frac{1}{R} \frac{\partial w}{\partial s} \quad (3.8)$$

### 3.3 Constraints

Since the whole length of the tube is made up of several independent segments, which have their own local coordinate systems and variables, it is necessary to enforce compatibility of deformations at junction of two or more segments. Two constraint equations are used to ensure compatibility of displacements and one to ensure compatibility of rotation between two segments. Therefore, at a junction where M segments come together, 3(M-1) constraint equations need to be enforced. At a junction between two straight segments having orientation angle  $\theta_1$  and  $\theta_2$  and components

$u_1, w_1$  and  $u_2, w_2$ , the two displacement compatibility conditions can be written in terms of the displacement components in the Y and Z directions as follows:

$$u_2 \cos \theta_2 + w_2 \sin \theta_2 - u_1 \cos \theta_1 - w_1 \sin \theta_1 = 0 \quad (3.9)$$

$$u_2 \sin \theta_2 - w_2 \cos \theta_2 - u_1 \sin \theta_1 + w_1 \cos \theta_1 = 0 \quad (3.10)$$

The rotation constraint requires that the angle between segments at a junction remain unchanged. For the current example, if the rotations of the two members at the junction are  $\beta_1$  and  $\beta_2$ , compatibility condition is

$$\beta_2 - \beta_1 = 0 \quad (3.11)$$

## CHAPTER 4

### CONSTITUTIVE EQUATION

The elastic-plastic model, which has been implemented in the program, has been developed by Pourboghrat et al (2000). It is based on the isotropic hardening model. The uniaxial stress-plastic strain curve of the material is given by

$$\bar{\sigma} = K(\bar{\epsilon} + \bar{\epsilon}_0)^N \quad (4.1)$$

where  $\bar{\sigma}$  is the effective stress and  $\bar{\epsilon}$  is the plastic strain. Parameters  $K$ ,  $N$  and  $\bar{\epsilon}_0$  are material constants. The elastic strain increment is related to the stress increment through the equations of linear, isotropic elasticity with Young's modulus  $E$  and Poisson's ratio. The yield function allows for anisotropic yielding of the material. The yield function is given by

$$f = \frac{\sigma_x^2 + \sigma_s^2 + R(\sigma_x - \sigma_s)^2}{1 + R} - \sigma_y^2 = 0 \quad (4.2)$$

where  $\sigma_y$  is the yield stress and  $R$  is an anisotropy parameter.

During loading, Hooke's law is used to calculate stress below the elastic limit; i.e.,  $\bar{\sigma} \leq \sigma_y$ , where  $\sigma_y$  is the initial yield stress of the sheet obtained from a uniaxial tensile test. Beyond the elastic limit; i.e.,  $\bar{\sigma} > \sigma_y$ , the co-rotational time derivative of stress (Jaumann stress rate) is calculated, for a given strain rate, from an elasto-plastic constitutive equation (Becker, 1992):

$$\overset{\nabla}{\underset{\sim}{\sigma}} = \left[ \underset{\sim}{L} - \frac{\underset{\sim}{L} : \underset{\sim}{P} \underset{\sim}{P} : \underset{\sim}{L}}{\underset{\sim}{P} : \underset{\sim}{\sigma}} \right] : \underset{\sim}{D} \quad (4.3)$$

$$h \frac{\underset{\sim}{P} : \underset{\sim}{\sigma}}{\underset{\sim}{\sigma}} + \underset{\sim}{P} : \underset{\sim}{L} : \underset{\sim}{P}$$

Here  $\overset{\nabla}{\underset{\sim}{\sigma}}$  and  $\underset{\sim}{D}(=\underset{\sim}{D}^e + \underset{\sim}{D}^p)$  are the Jaumann rate of stress and strain rate tensors, respectively,  $\underset{\sim}{\sigma}$  is the stress tensor,  $\bar{\sigma}$  is the material flow strength,  $h(=\partial\bar{\sigma}/\partial\bar{\epsilon})$  is the plastic hardening parameter,  $\underset{\sim}{L}$  is the fourth order elastic tensor and  $\underset{\sim}{P}(=\partial\phi/\partial\underset{\sim}{\sigma}/\|\partial\phi/\partial\underset{\sim}{\sigma}\|)$ , where  $\|\partial\phi/\partial\underset{\sim}{\sigma}\| = \sqrt{\partial\phi/\partial\underset{\sim}{\sigma} : \partial\phi/\partial\underset{\sim}{\sigma}}$ , is the second order tensor representing the unit normal to the flow potential surface. The plastic strain rate, associated with Eq.(4.3), is calculated from the following expression:

$$\dot{\bar{\epsilon}} = \frac{\underset{\sim}{P} : \underset{\sim}{L} : \underset{\sim}{D} - \underset{\sim}{P} : \overset{\nabla}{\underset{\sim}{\sigma}}}{\frac{\bar{\sigma}}{\underset{\sim}{P} : \underset{\sim}{\sigma}} \underset{\sim}{P} : \underset{\sim}{L} : \underset{\sim}{P}} \quad (4.4)$$

The fourth order elastic tensor  $\underset{\sim}{L}(=L_{ijkl})$  used in this work is the standard tensor for the isotropic elasticity, which has only two independent components.

## **CHAPTER 5**

### **CONTACT ALGORITHM**

The simulation of hydroforming processes requires the ability to model the contact phenomena. The analysis of contact behavior is complex because of the requirement to accurately track the motion of multiple geometric bodies, and the motion due to the interaction of these bodies after the contact. The numerical objective is to detect the motion of the bodies, apply a constraint to avoid penetration, and apply appropriate boundary condition to simulate the frictional behavior (Marc's Theory and user information).

#### **5.1 Numerical Procedures for Contact**

Two widely used procedures are available, namely the Lagrange multiplier method and penalty method, which will be introduced here briefly. Both, the Lagrange multiplier method and penalty method operate on variational formulation of problem under consideration (Bathe, 1982).

For purpose of demonstration, consider the total potential energy  $\Pi_p$  of a discrete system for steady-state analysis,

$$\Pi_p = \frac{1}{2} \mathbf{U}^T \mathbf{K} \mathbf{U} - \mathbf{U}^T \mathbf{R} \quad (5.1)$$

The constraint equations can be expressed as

$$\mathbf{C} \mathbf{U} = 0 \quad (5.2)$$

In the Lagrange multiplier method we amend the r.h.s. of (5.1) to obtain

$$\Pi_p^* = \frac{1}{2} \mathbf{U}^T \mathbf{K} \mathbf{U} - \mathbf{U}^T \mathbf{R} + \lambda^T \mathbf{C} \mathbf{U} \quad (5.3)$$

where  $\lambda$  contains as many Lagrange multipliers as there are constraint equations, and invoke that  $\delta \Pi_p^* = 0$ , which gives

$$\begin{bmatrix} \mathbf{K} & \mathbf{C}^T \\ \mathbf{C} & \mathbf{0} \end{bmatrix} \begin{Bmatrix} \mathbf{U} \\ \boldsymbol{\lambda} \end{Bmatrix} = \begin{Bmatrix} \mathbf{R} \\ \mathbf{0} \end{Bmatrix} \quad (5.4)$$

The second of Eq.(5.4) is Eq.(5.2), the equation of constraint. Eq.(5.4) are solved for both  $\mathbf{U}$  and  $\boldsymbol{\lambda}$ . The  $\lambda_i$  may be interpreted as force of constraint.

In the penalty method we also amend the r.h.s. of (5.1) but without introducing an additional variable. Now we use

$$\Pi_p^* = \frac{1}{2} \mathbf{U}^T \mathbf{K} \mathbf{U} - \mathbf{U}^T \mathbf{R} + \frac{1}{2} \mathbf{t}^T \boldsymbol{\alpha} \mathbf{t} \quad (5.5)$$

in which  $\mathbf{t} = \mathbf{C} \mathbf{U}$ , and  $\mathbf{t} = \mathbf{0}$  implies satisfaction of the constraint. The usual potential  $\Pi_p$

of the system can be augmented by a penalty function  $\frac{1}{2} \mathbf{t}^T \boldsymbol{\alpha} \mathbf{t}$ , where  $\boldsymbol{\alpha}$  is a diagonal matrix of penalty numbers  $\alpha_i$ . The condition  $\delta \Pi_p^* = 0$  now yields

$$[\mathbf{K} + \mathbf{C}^T \boldsymbol{\alpha} \mathbf{C}] \mathbf{U} = \mathbf{R} \quad (5.6)$$

If  $\boldsymbol{\alpha} = \mathbf{0}$ , the constraints are ignored. As  $\boldsymbol{\alpha}$  grows,  $\mathbf{U}$  changes in such a way that the constraint equations are more nearly satisfied.

It is difficult to assess which method, the Lagrange multiplier method and penalty method, is better in the finite element implementation. However, it can be mentioned that the Lagrange multiplier method introduces a large number of independent variables. Also, the diagonal terms of the stiffness matrix corresponding to the  $\lambda$  always become zero and special attention is required during the assembly of the stiffness matrix so that an equation corresponding to any  $\lambda$  does not become the first one in the stiffness

equations after applying the boundary conditions (Kobayashi et al, 1989). In comparison with Lagrange multiplier, penalty functions have the advantages of introducing no new variables and requiring no special care for the order of unknowns for successful equation solving. Their implementation can be as easy as assigning a high modulus for an element already in the program. Thus, we use penalty functions to implement the constraints in contact problem.

Effectively, the penalty procedure constrains the motion by applying a penalty to the amount of penetration that occurs in the hydroforming processes. The penalty approach can be considered as analogous to a nonlinear spring between the two bodies. Using the penalty approach, some penetration occurs with the amount being determined by the penalty constant or function. The choice of the penalty value can also have a detrimental effect on the numerical stability of the global solution procedure.

## **5.2 Detection of Contact**

During the contact process, each potential contact node is first checked to see whether it is near a contact segment. The contact segments are either edges of the other 2D deformable bodies, faces of 3D deformable bodies, or segments from rigid bodies that stand for the dies in tube hydroforming process. The motion of the nodes is checked to see whether it has penetrated a surface by determining whether it has crossed a segment. The determination of when contact occurs and the calculation of the normal vector are critical to the numerical simulation. In this part, the normal vector of potential contact node has been pre-defined and a so-called cross-product algorithm is used to determine which segment is associated with the potential contact node.



### 5.2.1 Contact Tolerance

During the contact process, it is unlikely that a node exactly contact the surface. For this reason, a contact tolerance is associated with each surface (Figure 5.1). If a node is within the contact tolerance, it is considered to be in contact with the segment. The contact tolerance is calculated by the program as 5% of the thickness of segment.

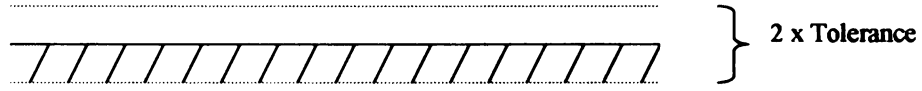


Figure 5.1 Contact tolerance

### 5.2.2 Normal Vector and Tangential Vector

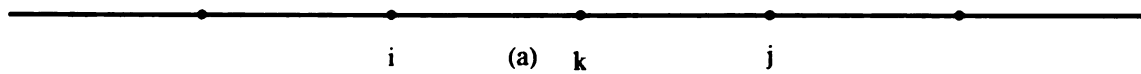
In order to track the motion of each potential contact node, it is important to define the normal vector and tangential vector of the node (Sheet-S).

The normal and tangential vectors of the nodes of the mesh (Figure 5.2(a)) can be calculated as follows: The element  $i$  has nodes  $i$  and  $k$  and length  $L_i$ , The element  $j$  has nodes  $k$  and  $j$  and length  $L_j$ . The unit normal vector,  $\mathbf{n}$ , at the contact node  $k$ , as shown in Figure 5.2(b), is evaluated by averaging the normals of elements  $i$  and  $j$ ,  $\mathbf{N}_i$  and  $\mathbf{N}_j$ , as follows:

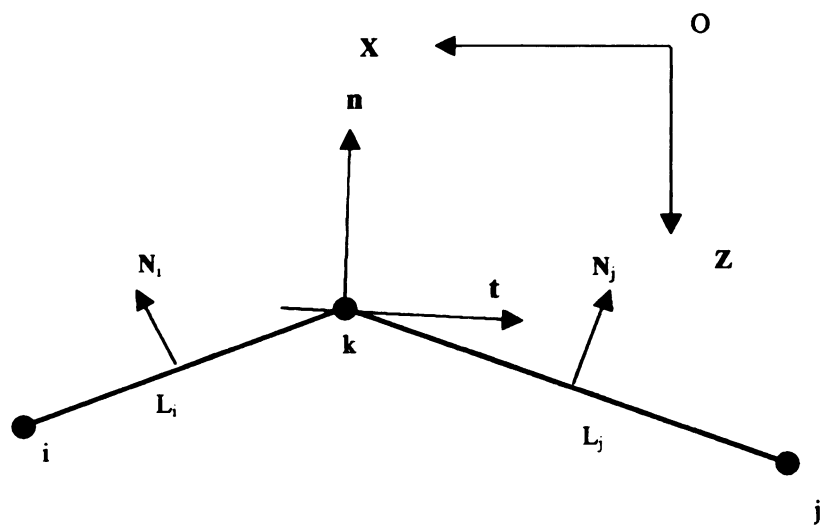
$$\mathbf{n} = \frac{\mathbf{N}_i + \mathbf{N}_j}{\|\mathbf{N}_i + \mathbf{N}_j\|} \quad (5.7)$$

By rewriting the normal vector,  $\mathbf{n}$ , in the following component form:

$$\mathbf{n} = \frac{1}{ZN} \begin{Bmatrix} Z_x \\ -1 \end{Bmatrix}; \quad ZN = \sqrt{Z_x^2 + 1} \quad (5.8)$$



(a)



(b)

Figure 5.2 (a) The computational mesh and

(b) The normal vector and tangent vector

where  $Z_x$  which is interpreted as the slope at node k, can be obtained from Eq.(5.7), in terms of the coordinates,  $(x,z)$ , of the nodes i, k and j, as follows:

$$Z_x = \frac{L_j(z_k - z_i) + L_i(z_j - z_k)}{L_j(x_k - x_i) + L_i(x_j - x_k)} \quad (5.9)$$

where  $L_i$  and  $L_j$  are respectively lengths of elements i and j. As seen in Eqs(5.8) and (5.9), the normal vector,  $\mathbf{n}$ , at the contact node k, can be expressed in terms of the neighboring nodal coordinates.

The tangent unit vector,  $\mathbf{t}$ , at the node k, whose direction is normal to the normal vector,  $\mathbf{n}$ , and which is oriented opposite to the sliding direction, is expressed using the orthogonality as follows:

$$\mathbf{t} = \frac{1}{ZN} \begin{Bmatrix} 1 \\ Z_x \end{Bmatrix} \quad (5.10)$$

where  $ZN$  and  $Z_x$  are defined in Eq.(5.8) and Eq.(5.9), respectively.

Actually, as we can see in Appendix B, when the Fourier series expansion is used to approximate the nodal coordinates, it is easy to exactly define the normal of a node by differentiating the Fourier series without any numerical difficulty.

### 5.2.3 Condition for Contact Violation

As shown in Figure 5.3, when a node is within the contact tolerance, it is considered to be in contact with the segment. The location of the closest point on the die corresponding to the contact node needs to be determined by using the cross-product algorithm.  $B_{i-1}$ ,  $B_i$  and  $B_{i+1}$  are die nodes,  $A_k$  is one of the contact nodes and  $\mathbf{n}$  is its normal vector.

$$\text{If } (\overrightarrow{A_k B_{i-1}} \times \mathbf{n}) \cdot (\overrightarrow{A_k B_i} \times \mathbf{n}) > 0 \quad (5.11a)$$

$$\text{and } (\overrightarrow{A_k B_i} \times \mathbf{n}) \cdot (\overrightarrow{A_k B_{i+1}} \times \mathbf{n}) < 0 \quad (5.11b)$$

Then, we define segment  $B_i B_{i+1}$  to be the segment associated with contact node  $A_k$ .

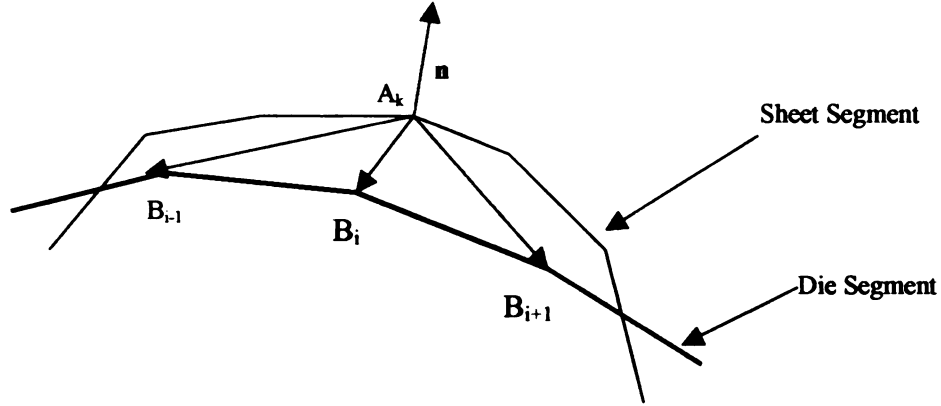


Figure 5.3 The associated die segment with contact node

### 5.3 The Projection Algorithm

A nodal position produced by the trial solution may penetrate the die. By using the cross-product algorithm, the closest point on the die corresponding to the node can be found. The nodal coordinates are then modified by a projection scheme such that the node just touches the die surface. There are two ways to bring the penetrated node back to the die surface.

#### 5.3.1 The Iterative Method

The position of a penetrated node is changed to locate it at the tool (die) surface where the normal vector for that node intersects it. After calculating the normal vector,  $\mathbf{n} = (n_x, n_z)$ , using Eq.(5.8), the tool surface point to be projected  $(t \cdot n_x, t \cdot n_z)$  can be iteratively found by solving for the length parameter,  $t$ , from the nonlinear equation:

$$S(t \cdot \mathbf{n}_x) - t \cdot n_z = 0 \quad (5.12)$$

where  $S(x)$  is the tool surface equation.

### 5.3.2 The Directive Method

As shown in Figure 5.4, PQ is assumed to be the tool segment associated with the penetrated node A, point B is the intersection point between normal vector and PQ , and O is the original point. Based on the following vector equation, the coordinate of point B could be calculated:

$$\overrightarrow{OP} + \overrightarrow{PB} = \overrightarrow{OA} + \overrightarrow{AB} \quad (5.13a)$$

$$\overrightarrow{PB} = \eta_1 \frac{\overrightarrow{PQ}}{\|\overrightarrow{PQ}\|}, \quad \overrightarrow{AB} = -\eta_2 \mathbf{n} \quad (5.13b)$$

where  $\eta_1, \eta_2$  are scalar. Once  $\eta_1, \eta_2$  are solved from Eq.(5.13), the coordinate of B could be determined.

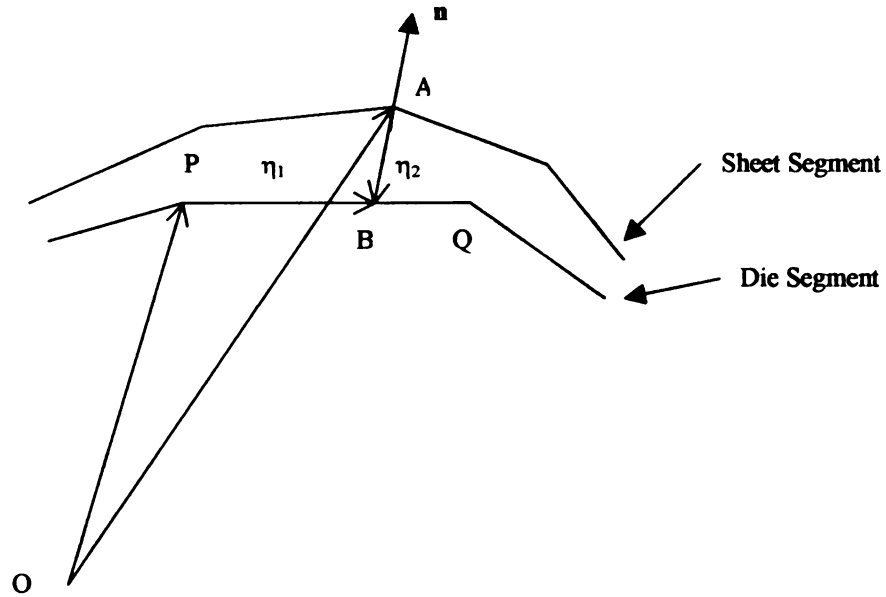


Figure 5.4 The projection Algorithm

## 5.4 Implementation of Constraint

A node located on the sheet at time  $t + \Delta t$ , is constrained to move in the tangent direction defined by the trial solution,  $\Delta \mathbf{u}^*$ . The tangent direction incorporates the  $Z_x$  in Eq.(5.9). The constraint on  $\delta \mathbf{u} = (\delta u_x, \delta u_z)$ , for contacting nodes is then:

$$\delta \mathbf{u} \cdot \mathbf{n} = 0 \quad (5.14)$$

which by substituting in Eq.(5.8) we will have

$$\delta u_z = Z_x \cdot \delta u_x \quad (5.15)$$

Actually, Eq.(5.15) is the alternative constraint equation, Eq.(5.2), in the contact problem.

## 5.5 Friction Model

Friction is a complex physical phenomenon that involves the characteristics of the surface such as surface roughness, temperature, normal stress, and relative velocity. The numerical modeling of the friction has been simplified to two idealistic models.

The most popular friction model is the Coulomb Friction model. This model is used for most applications. The Coulomb model (Marc's Theory and user information) is:

$$\sigma_{fr} \leq -\mu \sigma_n \cdot \mathbf{t} \quad (5.16)$$

where  $\sigma_n$  is the normal stress

$\sigma_{fr}$  is the tangential(friction) stress

$\mu$  is the friction coefficient

$\mathbf{t}$  is the tangential vector in the direction of the relative velocity

$\mathbf{t} = \frac{\mathbf{v}_r}{|\mathbf{v}_r|}$ ,  $\mathbf{v}_r$  is the relative sliding velocity.

The Coulomb model is also often written with respect to forces

$$\mathbf{f}_t \leq -\mu \mathbf{f}_n \cdot \mathbf{t} \quad (5.17)$$

where  $\mathbf{f}_t$  is the tangential force,  $\mathbf{f}_n$  is the normal reaction.

For a given normal stress, the friction stress has a step function behavior based upon the value of  $\mathbf{v}_r$  (see Figure 5.5).

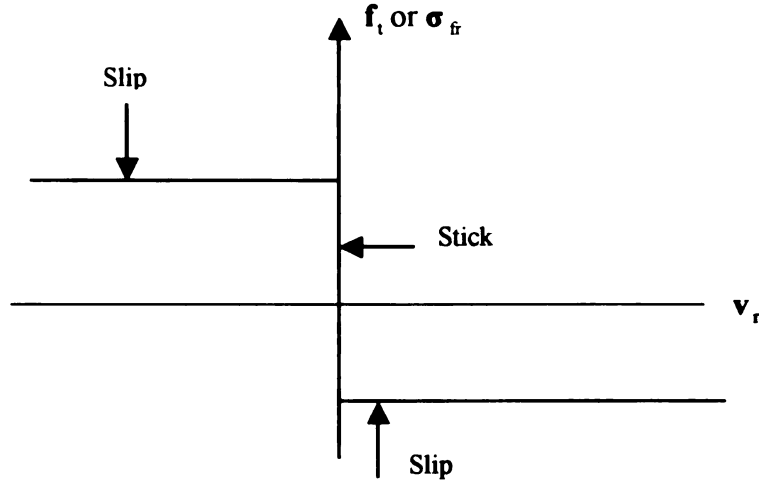


Figure 5.5 Coulomb Friction Model

This discontinuity in the value of  $\sigma_{fr}$  can result in numerical difficulties so a modified Coulomb friction model (Oh, 1982) is implemented:

$$f_s = -mk \frac{\Delta v_s}{|\Delta v_s|} \approx -\frac{2}{\pi} mk \tan^{-1} \left( \frac{\Delta v_s}{u_0} \right) \quad (5.18)$$

where  $\Delta v_s$  is slipping velocity,  $m$  is friction factor,  $k$  local flow stress in shear and  $u_0$  is very small positive number compared to  $\Delta v_s$ .

When the Coulomb model is used with the stress based model, the integration point stresses are used to calculate the normal stress component of the contact node. The tangential stress is then evaluated and a consistent nodal force is calculated.

## **5.6 Separation**

After a node comes into contact with a surface, it is possible for it to separate in a subsequent iteration or increment. Mathematically, a node should separate when the reaction force between the node and surface becomes tensile or positive.

When contact occurs, a reaction force associated with the node in contact balance the internal stress of the element adjacent to this node. When separation occurs, this reaction force behaves as a residual force (as the force on a free node should be zero). This requires that the internal stresses in the deformable body be redistributed.



## CHAPTER 6

### NUMERICAL SIMULATION

In this chapter, based on the virtual work principle, the equilibrium equation can be derived. The numerical solution obtained from a Total Lagrangian formulation of a general thin shell theory is employed. In contrast to traditional finite element method, the nodal displacement approximate function based on Fourier series is used. The boundary friction condition is introduced into the formulation in the form of penalty function, which imposes the constraints directly into the tangent stiffness matrix. The Newton-Raphson algorithm is used to solve the nonlinear equilibrium equation.

#### 6.1 Principle of Virtual Work

An equivalent approach to express the equilibrium of the body is to use the principle of virtual work. This principle states that the equilibrium of the body requires that for any compatible, small virtual displacements imposed onto the body, the total internal virtual work is equal to total external virtual work. In the Lagrangian incremental analysis approach we express the equilibrium of the body at time  $t + \Delta t$  using the principle of virtual work as:

$$\int_{t+\Delta t_V} {}^{t+\Delta t}\tau_{ij} \delta {}^{t+\Delta t}e_{ij} {}^{t+\Delta t}dV = \int_{t+\Delta t_V} {}^{t+\Delta t}f_i^B \delta u_i {}^{t+\Delta t}dV + \int_{t+\Delta t_S} {}^{t+\Delta t}f_i^S \delta u_i^S {}^{t+\Delta t}dS \quad (6.1)$$

Where l.h.s is the total internal virtual work and r.h.s is total external virtual work. The  ${}^{t+\Delta t}\tau_{ij}$  are the Cartesian components of the Cauchy stress tensor, the  ${}^{t+\Delta t}e_{ij}$  are the Cartesian components of an infinitesimal strain tensor, the  ${}^{t+\Delta t}f_i^B$  and  ${}^{t+\Delta t}f_i^S$  are the components of the externally applied body and surface force vectors, respectively, and  $\delta u_i$  is the  $i$ th component of the virtual displacement vector.

## 6.2 Newton-Raphson Algorithm

Substituting the element coordinate and displacement interpolation into the principle of virtual work expression Eq.(6.1), the equilibrium equation can be written as

$${}^{t+\Delta t}\mathbf{R} - {}^{t+\Delta t}\mathbf{F} = 0 \quad (6.2)$$

where the vector  ${}^{t+\Delta t}\mathbf{R}$  lists the externally applied nodal point forces in the configuration at time  $t + \Delta t$ , and the vector  ${}^{t+\Delta t}\mathbf{F}$  lists the nodal point forces that correspond to the element stresses in this configuration. For the nonlinear problems, the basic approach for an incremental step-by-step solution is to assume that the solution for the discrete time  $t$  is known, and that the solution for the discrete time  $t + \Delta t$  is required, where  $\Delta t$  is a suitably chosen time increment. Hence, considering (6.2) at time  $t + \Delta t$  we have

$$\mathbf{f}(\mathbf{U}^*) = 0 \quad (6.3)$$

where 
$$\mathbf{f}(\mathbf{U}^*) = {}^{t+\Delta t}\mathbf{R}(\mathbf{U}^*) - {}^{t+\Delta t}\mathbf{F}(\mathbf{U}^*) \quad (6.4)$$

Assume that in the iterative solution we have evaluated  ${}^{t+\Delta t}\mathbf{U}^{(i-1)}$ ; then a Taylor series expansion gives

$$\mathbf{f}(\mathbf{U}^*) = \mathbf{f}({}^{t+\Delta t}\mathbf{U}^{(i-1)}) + \left[ \frac{\partial \mathbf{f}}{\partial \mathbf{U}} \right]_{t+\Delta t, \mathbf{U}^{(i-1)}} (\mathbf{U}^* - {}^{t+\Delta t}\mathbf{U}^{(i-1)}) \quad (6.5)$$

where higher-order terms are neglected. Substituting from (6.4) into (6.5) and using (6.3) we obtain

$$0 = {}^{t+\Delta t}\mathbf{R} - {}^{t+\Delta t}\mathbf{F}^{(i-1)} + \left[ \frac{\partial \mathbf{R}}{\partial \mathbf{U}} - \frac{\partial \mathbf{F}}{\partial \mathbf{U}} \right]_{t+\Delta t, \mathbf{U}^{(i-1)}} (\mathbf{U}^* - {}^{t+\Delta t}\mathbf{U}^{(i-1)}) \quad (6.6)$$

when we assume that the externally applied loads are independent of the displacements,

which means  $\left. \frac{\partial \mathbf{R}}{\partial \mathbf{U}} \right|_{t+\Delta t, \mathbf{U}^{(i-1)}} = 0$ , (6.6) becomes

$$\left[ \frac{\partial \mathbf{F}}{\partial \mathbf{U}} \right]_{t+\Delta t, \mathbf{U}^{(i-1)}} (\mathbf{U}^* - {}^{t+\Delta t} \mathbf{U}^{(i-1)}) = {}^{t+\Delta t} \mathbf{R} - {}^{t+\Delta t} \mathbf{F}^{i-1} \quad (6.7)$$

We now define

$$\Delta \mathbf{U}^{(i)} = \mathbf{U}^* - {}^{t+\Delta t} \mathbf{U}^{(i-1)} \quad (6.8)$$

and

$$\left. \frac{\partial \mathbf{F}}{\partial \mathbf{U}} \right|_{t+\Delta t, \mathbf{U}^{(i-1)}} = {}^{t+\Delta t} \mathbf{K}^{(i-1)} \quad (6.9)$$

where  ${}^{t+\Delta t} \mathbf{K}^{(i-1)}$  is the tangent stiffness matrix in iteration  $i-1$ , which we assume to be nonsingular. Thus (6.7) can be written as

$${}^{t+\Delta t} \mathbf{K}^{(i-1)} \Delta \mathbf{U}^{(i)} = {}^{t+\Delta t} \mathbf{R} - {}^{t+\Delta t} \mathbf{F}^{(i-1)} \quad (6.10)$$

Since (6.5) represents only a Taylor series approximation, the displacement increment correction is used to obtain the next displacement approximation

$${}^{t+\Delta t} \mathbf{U}^{(i)} = {}^{t+\Delta t} \mathbf{U}^{(i-1)} + \Delta \mathbf{U}^{(i)} \quad (6.11)$$

*The relation in (6.9) and (6.10) constitute the Newton-Raphson solution of (6.2).*

### 6.3 Four Types of Modeling

Four different models, i.e. for pressure loading, axial force, displacement stroke and frictional contact, are derived respectively.

#### 6.3.1 Pressure Loading Modeling

Based on kinematics and constitutive equation discussed in Chapter 3 and Chapter 4, the principle of virtual work is used to satisfy the equilibrium equation and takes the following form for pressure loading:

$$\sum_{i=1}^I \int_{L^i} (\sigma_x^i \delta \varepsilon_x^i + \sigma_{s_i}^i \delta \varepsilon_{s_i}^i) R^i dL^i + \sum_{j=1}^J \lambda_j \delta C_j = \delta W_{Ext}^P \quad (6.12)$$

where  $I$  is the number of segments along the tube length,  $J$  is the number of constraint equations,  $\lambda_j$  are Lagrange multipliers,  $C_j$  are the constraint equations (from Eqs.(3.9-3.11),  $\delta W_{Ext}^P$  is virtual work due to external force (pressure),  $dL^i$  is the incremental length for the straight segment and  $R^i$  is the radius of the tube at current segment.

The displacement component  $w_i, u_i$  for each straight segment are approximated using the following Fourier series expressions:

$$w_i = \alpha_0^i + \sum_{n=1}^{N^i} \alpha_n^i \cos \frac{n\pi s_i}{l_i^0} + \sum_{n=1}^{N^i} \beta_n^i \sin \frac{n\pi s_i}{l_i^0} \quad (6.13a)$$

$$u_i = \gamma_0^i + \sum_{n=1}^{N^i} \gamma_n^i \cos \frac{n\pi s_i}{l_i^0} + \sum_{n=1}^{N^i} \delta_n^i \sin \frac{n\pi s_i}{l_i^0} \quad (6.13b)$$

After substituting from Eqs.(6.13a-b) into the principle of virtual work Eq.(6.12), a nonlinear expression of the following form will result

$$f(c, P) = 0 \quad (6.14a)$$

where

$$c = \{\alpha_0^i, \alpha_n^i, \beta_n^i, \gamma_0^i, \gamma_n^i, \delta_n^i, \lambda_j\} \quad (6.14b)$$

Eq. (6.14) should be solved for  $c$  for given values of  $P$ .

Since Eq. (6.14) is highly nonlinear, it will be numerically solved by the Newton-Raphson method. The Newton-Raphson iterative method used to solve  $c$  will look like this:

$$[K] \delta c = [R] = F_{Ext} - F_{Int} \quad (6.15)$$

where  $K$  is the stiffness matrix,  $\delta c$  is the incremental  $c$  and  $R$  is the force residual.

$F_{Ext}$  is externally applied nodal forces,  $F_{Int}$  is the nodal forces that correspond to the element stress in this configuration ( Internal forces).

Pressure loading is modeled as an external force to expand the tube. The external work done by a pressure  $p$  applied to the inside of the tube is equal to

$$\delta W_{Ext}^P = \sum_{i=1}^I \int_{L_p^i} p \hat{n}^i \delta(\Delta u^i) R^i dL_p^i = \sum_{i=1}^I \int_{L_p^i} p \hat{n}^i \frac{\partial(\Delta u^i)}{\partial c} \delta c R^i dL_p^i \quad (6.16)$$

where  $\delta(\Delta u^i)$  is the virtual displacement increment having two components  $\delta(\Delta w^i)$  and  $\delta(\Delta v^i)$ ,  $\hat{n}^i$  is the unit outward normal to the segment  $L_p^i$ .

The variation of the virtual external work due to internal pressure loading is

$$F_{Ext}^P = p \sum_{i=1}^I \int_{L_p^i} \hat{n}^i \frac{\partial(\Delta u^i)}{\partial c} R^i dL_p^i \quad (6.17)$$

Due to the follower forces effect (Hibbitt, 1979), the load stiffness matrix is

$$K_{Ext}^P = p \sum_{i=1}^I \int_{L_p^i} \left( \frac{\partial(\hat{n}^i)}{\partial c} \frac{\partial(\Delta u^i)}{\partial c} + \hat{n}^i \frac{\partial^2(\Delta u^i)}{\partial^2 c} \right) R^i dL_p^i \quad (6.18)$$

Eq. (6.17) and (6.18) will appear on the right-hand and left-hand side of the Newton-Raphson expression (Eq. (6.15)) respectively, namely,

$$\left[ K + K_{Ext}^P \right] [d c] = [R] = F_{Ext} + F_{Ext}^P - F_{Int} \quad (6.19)$$

When we implemented above formulations into the code, we found that the load stiffness matrix  $K_{Ext}^P$  has nearly no effects on the solution that led us to simplify the

formulation. Actually, if we approximated  $\hat{n}^i \delta(\Delta \underline{u}^i) \approx \delta(\Delta \underline{w}^i)$ , the whole formulation

above can be simplified. The proof can be seen in Appendix B. Since  $\frac{\partial^2 (\Delta \underline{w}^i)}{\partial^2 \underline{c}} = 0$ , there

will be no stiffness matrix due to pressure ( $K_{Ext}^p$ ) going to the left side of the Newton-

Raphson expression (Eq. (6.19)). Both methods are implemented in the code; the results are almost the same.

### 6.3.2 Axial Loading

Application of axial force with internal pressure is critical to improve material shaping abilities for deeper draw configurations and higher expansion in localized regions. Axial compressive feed  $F$  is modeled as an external force at both the ends of the tube as follows:

$$\delta W_{Ext}^A = (-1)^k F \hat{t}^i \delta(\Delta \underline{u}^i) \Big|_{i=1, k=0}^{i=nseg, k=1} = (-1)^k F \hat{t}^i \frac{\partial (\Delta \underline{u}^i)}{\partial \underline{c}} \delta \underline{c} \Big|_{i=1, k=0}^{i=nseg, k=1} \quad (6.20)$$

where  $\delta(\Delta \underline{u}^i)$  is the virtual displacement increment having two components  $\delta(\Delta \underline{w}^i)$  and  $\delta(\Delta \underline{v}^i)$ ,  $\hat{t}^i$  is the unit tangent vector along the segment  $L_p^i$  and  $nseg$  is total number of segments. Since the force is compressive at both ends, when  $i = 1$  (i.e. first segment),  $k = 0$  and when  $i = nseg$  (i.e. last segment),  $k = 1$ .

### 6.3.3 Displacement Stroke Modeling

The displacement stroke at both ends of the tube is included in the equilibrium equation using Lagrange Multiplier technique. The stroke is specified in the  $\underline{u}$  direction (along the length of the tube).

For the left end of the tube ( $i = 1$ ):

$$\begin{aligned}
u|_{s=0, i=1} &= u^* \\
\Rightarrow \left( \gamma_0^i + \sum_{n=1}^{N^i} \gamma_n^i \cos \frac{n\pi s_i}{l_i^0} + \sum_{n=1}^{N^i} \delta_n^i \sin \frac{n\pi s_i}{l_i^0} \right) \Big|_{s=0, i=1} &= u^* \\
\Rightarrow \gamma_0^1 + \sum_{n=1}^{N^1} \gamma_n^1 &= u^* \\
\Rightarrow \gamma_0^1 + \sum_{n=1}^{N^1} \gamma_n^1 - u^* &= 0
\end{aligned} \tag{6.21}$$

For the right end of the tube ( $i = nseg$ ):

$$\begin{aligned}
u|_{s=l, i=nseg} &= -u^* \\
\Rightarrow \left( \gamma_0^i + \sum_{n=1}^{N^i} \gamma_n^i \cos \frac{n\pi s_i}{l_i^0} + \sum_{n=1}^{N^i} \delta_n^i \sin \frac{n\pi s_i}{l_i^0} \right) \Big|_{s=l, i=nseg} &= -u^* \\
\Rightarrow \gamma_0^{nseg} + \sum_{n=1}^{N^{nseg}} (-1)^n \gamma_n^{nseg} &= -u^* \\
\Rightarrow \gamma_0^{nseg} + \sum_{n=1}^{N^{nseg}} (-1)^n \gamma_n^{nseg} + u^* &= 0
\end{aligned} \tag{6.22}$$

Eqn. (6.21) and Eqn. (6.22) are incorporated in the equilibrium equation using two Lagrange Multipliers.

### 6.3.4 Frictional Contact Modeling

The most challenging task when developing a numerical code for metal forming processes is to model frictional contact. To model the tooling-workpiece frictional contact correctly, the following two conditions must be continually checked during each equilibrium iteration:

1. Penetration of the workpiece nodes into the tooling.
2. Nodal contact forces becoming tensile at the contact boundary (separation).

Once the penetration of the workpiece nodes into the tooling has been detected, the penetration nodes must be returned to the tooling surface and constrained to stay on the tooling surface for the remainder of the equilibrium iterations. The nodes, which are returned to the tooling surface, are constrained to move only tangent to the tooling surface and only condition 2 stated above can cause a contacting node to be detached from the tooling surface. Figure 6.1 shows an example of a typical contact check during the Newton-Raphson equilibrium iteration.

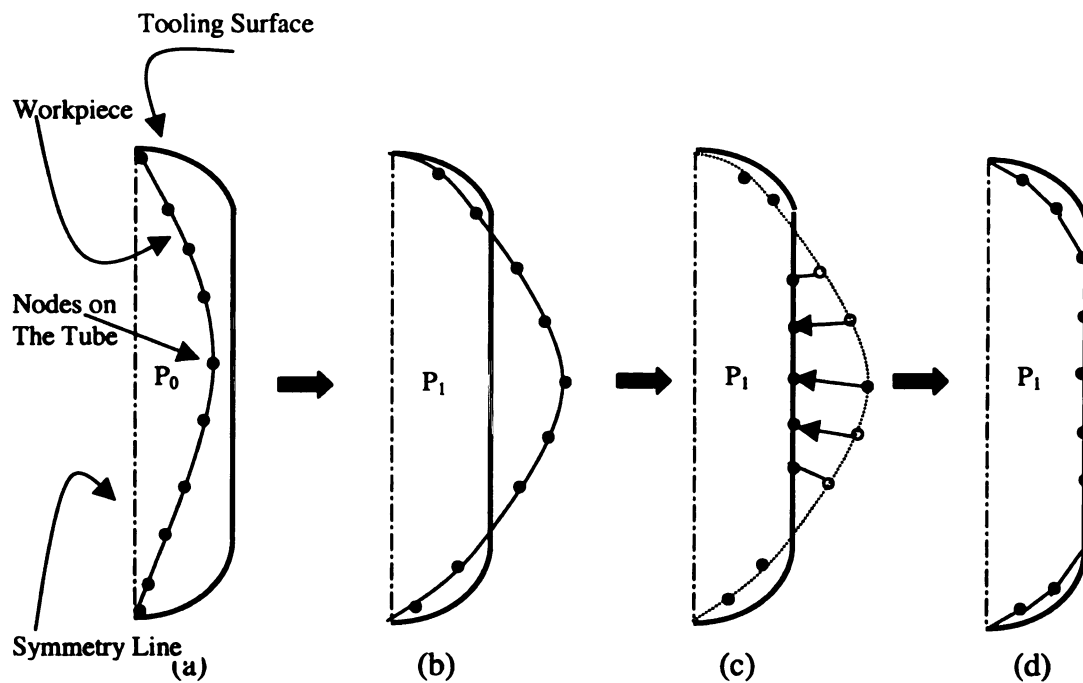


Figure 6.1 A schematic of tool-workpiece contact check

(a) shows the tube and the tooling, (b) shows initial penetration of some of the nodes, (c) shows how those nodes are returned to the tooling surface and finally (d) shows how the equilibrium shape is obtained after several iterations.



The external work done by the frictional contact is added into the virtual work principle equation (6.12) as following:

$$\sum_{i=1}^I \int_{L^i} (\sigma_x^i \delta \varepsilon_x^i + \sigma_{s_i}^i \delta \varepsilon_{s_i}^i) R^i dL^i + \sum_{j=1}^{J+2} \lambda_j \delta C_j =$$

$$(-1)^k \hat{F} \hat{t}^i \delta(\Delta \mathbf{u}^i) \Big|_{i=1, k=0}^{i=nseg, k=1} + p \sum_{i=1}^I \int_{L^i} \hat{n}^i \frac{\partial(\Delta \mathbf{u}^i)}{\partial c} R^i dL_p^i + \sum_{i=1}^I \int_{L^i} \tau_i \delta(\Delta \mathbf{u}^i) R^i dL_p^i \quad (6.23)$$

where  $\tau_i$  is the traction on the surface of the tube and  $\delta(\Delta \mathbf{u}^i)$  is the virtual incremental displacement of the contacting nodes.

In order to improve convergence, a special algorithm is introduced (see Figure 6.2). For each trial set of contacting and non-contacting nodes, equilibrium iteration is performed. After equilibrium is satisfied, the nodes are reexamined for non-penetration condition. The contact set is then updated by releasing or projecting certain nodes and another equilibrium iteration is initiated.

In each contact iteration, the trial displacements are first updated according to the Newton-Raphson procedure and the non-penetration contact condition is then applied to these trial values by projecting the contact nodes to the tool surface along the normal vector. The modified trial solutions are used for Newton-Raphson iteration. Within this force equilibrium iteration, the internal force is calculated. The signs of the sheet normal force at contact points are checked so that the nodes having non-compressive force are released.

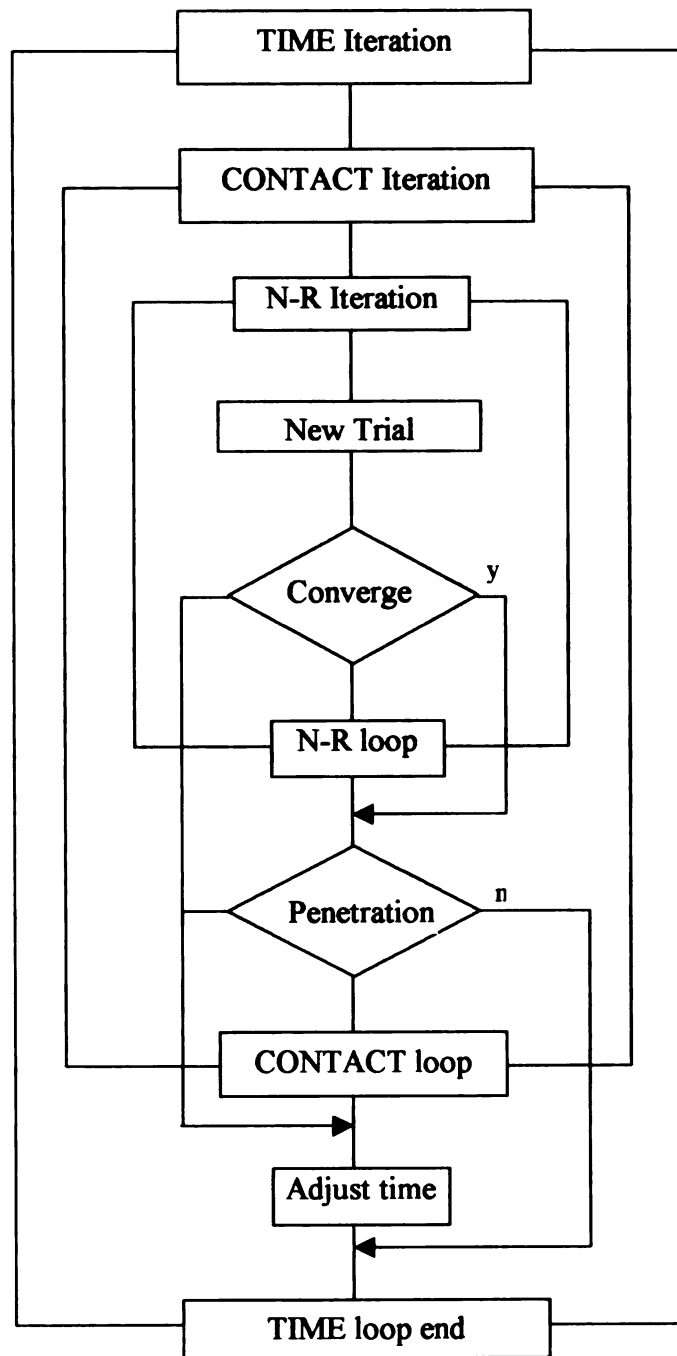


Figure 6.2 Flow chart for contact iteration

## 6.4 Fracture Criteria

Force Limiting Curve equations based on the onset of shear instability and on experimental measurements are incorporated in the program as fracture criteria:

### 6.4.1 Shear Instability:

Force Limiting Diagram based on the onset of local shear instability, using Hosford yield criterion and critical shear stress under plane strain (Lee & Kim, 1989), is given by:

$$\varepsilon_1^* = 2^{-\left(\frac{1}{n}\right)} \left[ 1 + \left( \frac{1}{|\beta|} \right)^a + R \left| 1 - \frac{1}{\beta} \right|^a \right]^{\frac{(na - n - 1)}{na}} \left[ 1 + R \left( 1 - \frac{1}{\beta} \right)^{-1} \left| 1 - \frac{1}{\beta} \right|^a \right]^{-1}$$

$$\left( 1 + |\alpha|^a + R |1 - \alpha|^a \right)^{1 - \frac{na + n}{na}} \left[ 1 + R(1 - \alpha)^{-1} |1 - \alpha|^a \right] (2 + \rho)^{1/n} (1 + \rho)^{-1/2n} (\varepsilon_{1p}^*) \quad (6.24)$$

where

$R$  = Anisotropy parameter

$n$  = Strain Hardening Exponent

$\alpha$  = Stress ratio

$\rho$  = Strain ratio

$\beta = 1 + R^{\frac{1}{1-a}}$

$a$  = Order of Yield Function (=2 for Yield Function used)

$\varepsilon_1^*$  = Maximum principal strain at shear instability

$\varepsilon_{1p}^*$  = Maximum principal strain from plane strain test

The effects of thickness, surface roughness and strain gradient through the thickness are not accounted for in the equation above.

#### **6.4.2 Experimental Measurements:**

The Force Limiting Curve derived from experimental measurements for Hot-dip galvanized DP600 (Asnafi, 1999) is used for Steel in the second verification problem.

## **CHAPTER 7**

### **PROGRAM STRUCTURE**

This chapter describes the input file, control flow of the main program and the output files.

#### **7.1 Input File**

The input is divided into two parts. The first part contains all the geometric, numerical and material information for a run. It is written in an input file that is read by the program prior to specification of the loading. The second part contains the loading history. This input is provided interactively by the user. All input is free-formatted.

##### **7.1.1 Geometric, Numerical and Material Input**

###### **1. Title of this case**

**TITLE**

**TITLE:** Array of 72 characters used to identify a case.

###### **2. Number of nodes**

**NODES, RADIUS**

**NODES:** Number of nodes in the cross-section. Each segment in the cross-section is bounded by two nodes. Maximum: 20.

**RADIUS:** Tube radius

###### **3. Node coordinates.** Input this record NODES times before proceeding to 4.

**YN, ZN**

**YN:** Y global coordinate of the location of this node.

**ZN:** Z global coordinate of the location of this node.

**4. Number of segments.**

**NSEG, MU, DELTAV**

**NSEG:** Total number of segments in the cross-section. The segment may be straight lines or circular arcs. Maximum: 40.

**MU:** The frictional factor.

**DELTAV:** The relative sliding velocity

**5. Type of segment.** Input NSEG item {5,6} pairs before proceeding to 7.

**STYPE**

**STYPE:** Enter “str” if the segment being described is straight.

**6. Segment parameters.**

For straight segments input the following record:

**INODE, JNODE, T, NCOEFF, IS, IZ, NC**

**INODE:** First node of the segment ( $s=0$ ).

**JNODE:** Second node of the segment ( $s=l_0$ ).

**T:** Thickness of the segment ( $t$ ).

**NCOEFF:** Number of terms in the Fourier series expansions for the displacement components ( $N$ ). Maximum: 10. Recommended: 4 to 6.

**IS:** Number of Gauss integration points along the segment. Maximum: 48. Recommended: 8 to 12.

**IZ:** Number of Gauss integration points along thickness of the segment. Maximum: 48. Recommended: 3 to 7.

**NC:** Number of contact nodes on segment (t).

**7. Number of point constraints**

**NPC**

**NPC:** Number of point constraints. At least three constraints are needed to prevent rigid body motion. Also input the constraints needed to maintain contact with the mandrel or symmetry conditions. All constraints are enforced at nodes.

**8. Point constraint information.** Input this record **NPC** times before proceeding to 9.

**NSPC, IVARPC**

**NSPC:** Segment number for which the point constraint will be enforced.

- If **NSPC** is positive, the constraint is enforced at the node with  $s = 0$ .
- If **NSPC** is negative, the constraint is enforced at the node with  $s = l_0$ .

**IVARPC:** Variable which will be constrained.

- To constrain the rotation  $\beta$ , input 1.
- To constrain the displacement component  $u$ , input 2.
- To constrain the displacement component  $w$ , input 3.

**9. Iteration parameters:**

**TOL, ITEMAX, JEVAL**

**TOL:** Convergence tolerance of Newton-Raphson iteration. Recommended: 0.00000001

**ITEMAX:** Maximum allowable number of iterations.

**JEVAL:** Multiple of the iteration count at which the Jacobian is evaluated. If **JEVAL** = 1 the Jacobian is evaluated every iteration, If **JEVAL** = 2 it is evaluated every other iteration, etc.

#### 10. Material properties.

<b>E, V, SIGMY, R, XK, XN, EPS0</b>
-------------------------------------

**E:** Young's modulus.

**V:** Poisson's ratio.

**SIGMY:** Initial yield stress.

**R:** Anisotropy parameter.

**XK:** Material constant.

**XN:** Hardening exponent.

**ESP0:** Initial plastic strain.

#### 11. Hardening Model.

<b>I_choice, A, B, C</b>
--------------------------

**I\_choice :**

- **I\_choice=1:** Ludwig-Holloman Model
- **I\_choice=2:** Voce's Model

**A, B, C :** Material constants for Voce's model



## 11. Output option.

<b>IWR</b>
------------

**IWR:**

- **IWR** = 1: print coefficients and Lagrange multipliers.
- **IWR** = 0: do not print coefficients and Lagrange multipliers.

### 7.1.2 Loading Input

Loading is prescribed in an incremental manner.

**Loading parameters**

<b>NINC, TINIT, TINC, PINC</b>
--------------------------------

**NINC:** Number of increments / Load-steps

**TINIT:** Initial Tension

**TINC:** Tension increment.

**PINC:** Internal pressure increment.

Displacement stroke increment is calculated by “*load\_curve.f*” based on the loading curve programmed.

### 7.2 Program Flow Chart

The program includes a main program and 24 subroutines.

Subroutine **input**: input geometric and material parameters.

Subroutine **store**: store integration, trigonometric and second derivative information.

Subroutine **newrap**: solve system of nonlinear equations using Newton-Raphson method.

Subroutine **build**: evaluate the system of equation and the Jacobian.

Subroutine **constr**: add constraint contribution to system of equation and Jacobian matrix.

...  
S  
S  
S  
Su  
Su  
Fol

Subroutine **decomp**: find the inverse matrix using Gauss-Jordan method.

Subroutine **disp**: evaluate displacements and their derivatives with respect to  $s$  at integration points along a segment.

Subroutine **dstrn** and **dstrnC**: derivatives of displacement components and their derivatives with respect to the coefficients of the series expansions at one point along  $s$  for straight and arc segment respectively.

Subroutine **d2curvature**: evaluate the second derivatives of curvature.

Subroutine **incm**: increment of all variables.

Subroutine **solve**: solve the nonlinear equations.

Subroutine **stndsp**: find strains at the integration points along the local coordinate.

Subroutine **stsstn**: find stress increments and force residual at integration points.

Subroutine **cnstutv**: constitutive equation.

Subroutine **contact**: deal with contact problem.

Subroutine **coloumb**: use Coloumb friction model.

Subroutine **dieinfo**: calculate die geometric information.

Subroutine **forcecheck**: check nodal force at each contact point.

Subroutine **getcoord**: calculate the coordinates of each integration point.

Subroutine **nodalf**: calculate nodal force at each contact point.

Subroutine **setpenalty**: set penalty function.

Subroutine **violation**: check each integration point to see if it violates contact.

Subroutine **bringback**: bring each contact point to die surface.

Subroutine **load\_curve.f**: calculates stroke increments based on current pressure.

Following is the flow chart of the program:

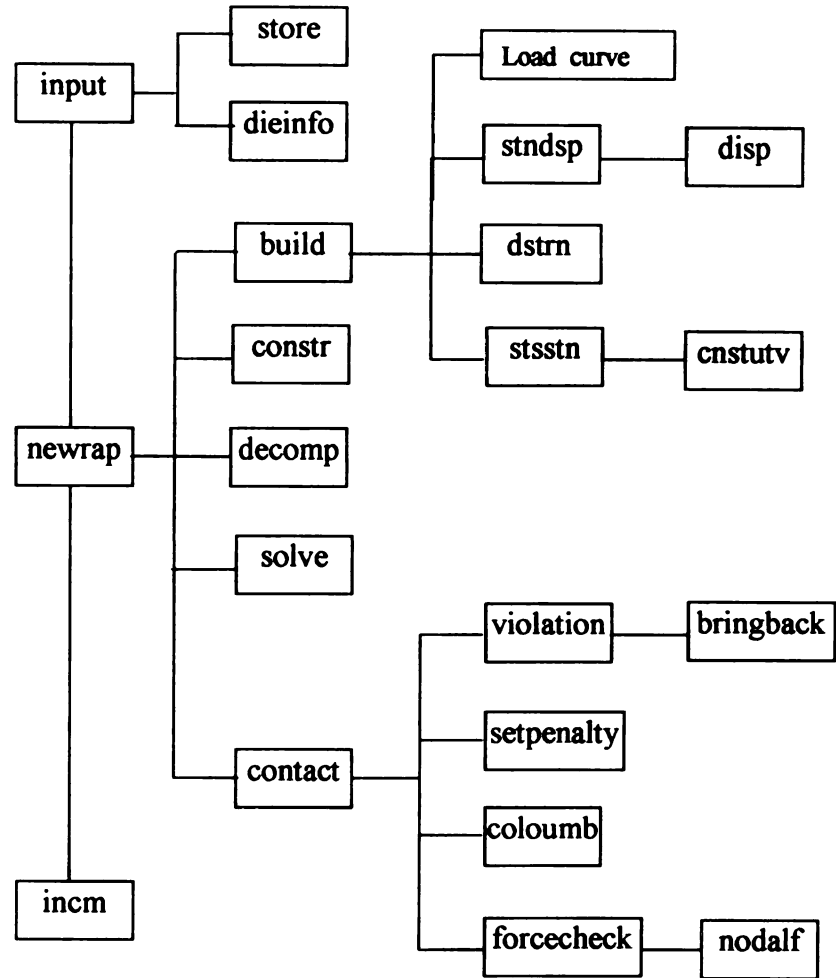


Figure 7.1 Flow chart of the program

S

I

F

L

of

the

Lir

Co

of f

### 7.3 Output File

The program has two output files: **betges.out** and **betges.coeff**. The contents of each file are described below:

**betges.out**: This file is formatted and contains the output of the program in the form of tables. The first part of this file is written prior to the specification of the loading and contains an augmented echo print of the input. It is useful to look at this part of the file to ensure that the input file was read correctly. The second part includes a list of the curvature, axial strain, tension and internal pressure at each loading step. If the variable **IWR** is set to 1 then the file will also contain the coefficients of the trigonometric series expansions for each segment.

**betges.coeff**: This file contains information necessary to make plot of the deformed cross-section of the member at any loading step. It also contains information to plot the shape of the meridian prior to loading. The file is organized as follows:

Line 1: (Format: i2)

Number of segments.

For each segment, the file contains the next set of three records:

Line 2.1: (i3, e13.5, a4, 3e13.5)

Number of terms in this segment, length of the segment, type of segment, location of the segment in  $Y$ , location of the segment in  $Z$ , radius of the segment. The location of the segment is partially given by the coordinates  $Y_0$  and  $Z_0$  as shown in Figure 3.2.

Line 2.2: (4e13.5)

Coordinates of the nodes bounding this segment in the following order:  $Y$ -coordinate of first node,  $Z$ -coordinate of first node,  $Y$ -coordinate of second node,  $Z$ -coordinate

c

c

in

st

Lin

Lin

For

of fo

Line

Line 3

Line 3

Line 3.3

(

of second node.

Line 2.3: (2e13.5)

Sine and cosine of the angle  $\theta$  defined in Figure 3.2 for straight segments. This concludes the part of this file which contains the original, undeformed description of the cross-section. The second part of the file contains, for each loading step, additional information necessary to describe the deformed shape of the meridian. For each loading step, the file contains the following:

Line 3.1: (i2)

Step number.

Line 3.2: (i2)

Segment number.

For each segment along the length of the tube, the output file contains the following set of four records:

Line 3.3.1: (6(e22.14))

$\alpha_0, (\alpha_n, n = 1, \text{number of terms}).$

Line 3.3.2: (6(e22.14))

$(\beta_n, n = 1, \text{number of terms}).$

Line 3.3.3: (6(e22.14))

$\gamma_0, (\gamma_n, n = 1, \text{number of terms}).$

Line 3.3.4: (6(e22.14))

$(\delta_n, n = 1, \text{number of terms}).$



7  
5  
4  
3  
2  
1  
0  
4,6  
str  
1,2  
str  
2,3  
str  
3,4  
str  
4,5,6  
3  
1,1  
1,3  
-4.2  
0.000  
10.3e

## CHAPTER 8

### EXAMPLES

The AXHD (Axisymmetric Hydroforming) program has been validated using the following two examples:

#### 8.1 Bulging of an Aluminium Tube

This example concerns bulging of a straight Aluminium tube under pressure and stroke loading. The tube is 8.0'' long with an outside diameter of 2.0'' and a wall thickness of 0.049''. The following are the material properties used for Aluminium 6061-T4 material in plasticity (Ludwig Holloman) model:

$E = 10300000$  psi,  $\nu = 0.3$ ,  $\sigma_y = 18730$  psi,  $R = 0.8179$ ,  $K = 69183$  psi,  $N = 0.2646$  and  $\epsilon_0 = 0$

The input file to run this case is shown below (the definition of input parameters at each line is given in Chapter 7):

```
Title: 'Aluminium Straight tube subject to 2030 psi pressure and 0.1181 in. stroke'
5,1,000
4,0,1,000
3,0,1,000
2,0,1,000
1,25,1,000
0,0,1,000
4,0,1,0,01,0
str
1,2,0.049,5,10,5,41
str
2,3,0.049,5,10,5,41
str
3,4,0.049,5,10,5,41
str
4,5,0.049,5,10,5,41
3
1,1
1,3
-4,2
0.000000001,150,1
10.3e6,0.3,18730,0.8179,69183,0.2646,0
```

1,0,0,0  
0

This tube was subjected to a pressure loading of 2030 psi and 0.1181'' axial displacement stroke. The deformed shape and strain results obtained from AXHD were compared with the results from ABAQUS and experimental measurements.

To study the effect of Aluminium's anisotropy on the strain distribution along the length of the tube, the ABAQUS code was run with the following three yield functions:

- Von Mises (Isotropic)
- Hills (with transverse anisotropy)
- Barlat (with planar anisotropy)

Due to the inability of ABAQUS/Standard to account for the current thickness and mid-surface offset for shell elements in contact analysis, the same simulation (with S4R shell element and Hill's yield function) was run with ABAQUS/Explicit and ABAQUS/Standard. The results were compared and it was found that the true strain distribution along the length of the tube is offset by a finite magnitude (within an acceptable error limit) when the mid-surface (instead of the external surface) contacts the die.

Figure 8.1 shows the intermediate shapes of the deformed tube predicted by AXHD program at various pressure levels. Similar to the experiment the tube was pressurized to the maximum pressure level of 2030 psi while axially being compressed to a maximum stroke of 0.1181'' (3.0 mm). The predicted deformed shape of the tube at the maximum pressure of 2030 psi is compared against the actual one. The radius of the predicted

deformed tube is 1.17" (29.72 mm), while that of the actual tube was measured to be 1.25" (31.75 mm). This corresponds to an underestimation of 6.4%.

Corresponding distribution of hoop and axial strains along the length of the tube are shown in figures 8.2 and 8.3. The maximum hoop and axial strains occur in the middle of the bulged tube and they are 17.54% and -7.4%, respectively. Figure 8.4 shows the thinning of the tube at the maximum bulge point (middle of the tube) as a function of the applied pressure. It is interesting to note that thinning accelerates exponentially beyond the pressure level of 1000 psi. The thinning strain at the pressure level of 2030 psi is 10%.

Figures 8.5 and 8.6 show a comparison of hoop and axial strain distributions predicted with AXHD code and ABAQUS/Explicit code using axisymmetric element (SAX1) and four-node shell element with reduced integration (S4R). The hoop strain distribution predicted by the AXHD code matches those of ABAQUS very well, despite the fact that a S4R shell element takes into account the shear deformation. Similarly, the axial strain distribution predicted by the AXHD code again matches those of ABAQUS very well. The two spikes (at  $\pm 1.5"$ ) shown in figure 8.6 for the ABAQUS/Explicit code are attributed to the dynamic effect.

Figure 8.7 shows a comparison of the measured and predicted hoop strain distribution, as a function of material models used. For comparison, in the numerical simulations isotropic and two types of anisotropic material models were used. Hill's yield criterion was reduced to Hosford yield criterion (Eqn. 4.2), for transverse anisotropy, for both SAX1 and S4R shell elements and then compared with AXHD results. Barlat's 1996

yield function was also used to account for planar anisotropy. As expected, the isotropic material model (von Mises) had the worst performance and significantly underestimated the magnitude of the maximum hoop strain (14.9%). Those models (Hill's SAX1, S4R and AXHD) accounting for transverse anisotropy showed some improvement but still underestimated the measured hoop strain (17.4%). Although not perfect, the best strain predictions were obtained with Barlat's yield function accounting for planar anisotropy (20.4%). The coefficients used in Barlat's yield function for the aluminum 6061-T4 tube were obtained from reference [Pourboghrat, F. et al., 2002]. The maximum hoop strain measured experimentally was about 25%. The high error percentage between the experimental and FEA results can be attributed to the high anisotropy of Aluminium. Also, the maximum attainable pressure in the used hydroforming equipment is 30,000 psi while the working range in Aluminium's case is 2000 psi. So, even an error of 0.5% (150 psi) in the pressure reading from the equipment will cause a high change in the strain and deformation results. This could account to the discrepancy in the simulation and experimental results too, since the experimental values obtained could well be for pressure beyond 2000 psi.

## **8.2 Steel Tube**

This example is concerned with the bulging of a straight steel tube under pressure and displacement stroke. The tube is 8.66'' long with an outside diameter of 2.36'' and a wall thickness of 0.05787''. The material properties used for hot-dip galvanized DP600 (HG/Z140) in plasticity (Ludwig Holloman) model are:

$E = 31465000$  psi,  $\nu = 0.3$ ,  $\sigma_y = 351040$  psi,  $R = 1.0$ ,  $K=143260$  psi,  $N=0.182$  and  $\epsilon_0=0$

2  
s  
3  
st  
4,  
st  
5,6  
str  
6,7  
3  
1,1  
1,3  
-6,2  
0.00  
31.4  
1,0,0  
0,0

simula  
(FLD),  
measur  
figures  
results for

The input file to run this case is shown below:

```
Title: 'DP600 isotropic material under 5220 psi pressure and 0.24 in. displacement stroke'
7,1,146
4.33,1.146
3.608,1.146
2.8867,1.146
2.165,1.146
1.4433,1.146
0.722,1.146
0.0,1.146
6,0.0,0.001,0
str
1,2,0.05787,6,12,7,41
str
2,3,0.05787,6,12,7,41
str
3,4,0.05787,6,12,7,41
str
4,5,0.05787,6,12,7,41
str
5,6,0.05787,6,12,7,41
str
6,7,0.05787,6,12,7,41
3
1,1
1,3
-6,2
0.000000000001,150,1
31.465e6,0.3,51040,1.0,143260,0.182,0
1,0,0,0
0,0
```

The stroke vs. pressure loading history and experimental results for this simulation are obtained from [Asnafi, N. et al, 1999]. The Forming Limit Diagrams (FLD), based on the onset of shear instability [Lee & Kim et al., 1989] and experimental measurements [Asnafi, N. et al, 1999] are used as fracture criteria. As shown in the figures described below, the results from AXHD are very close to the experimental results for this isotropic material.

t

h

Ti

axi

sho

mea

(FL

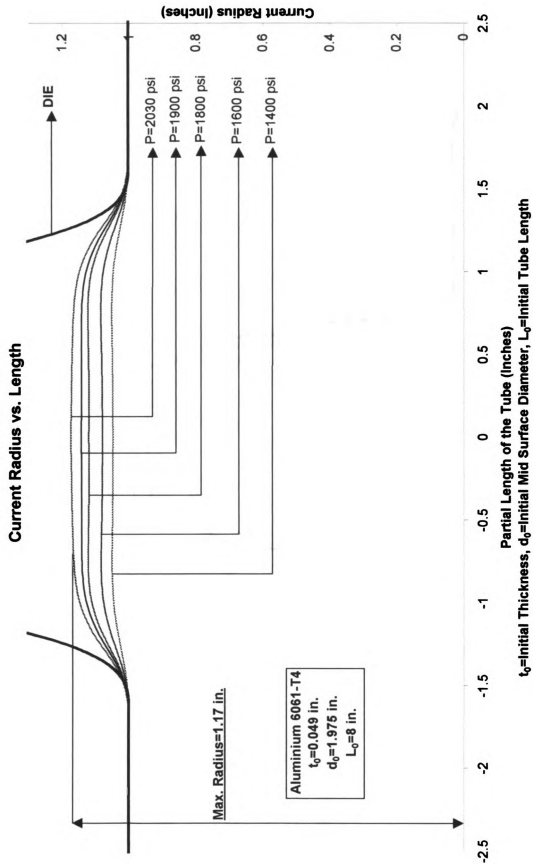
of 52

middl

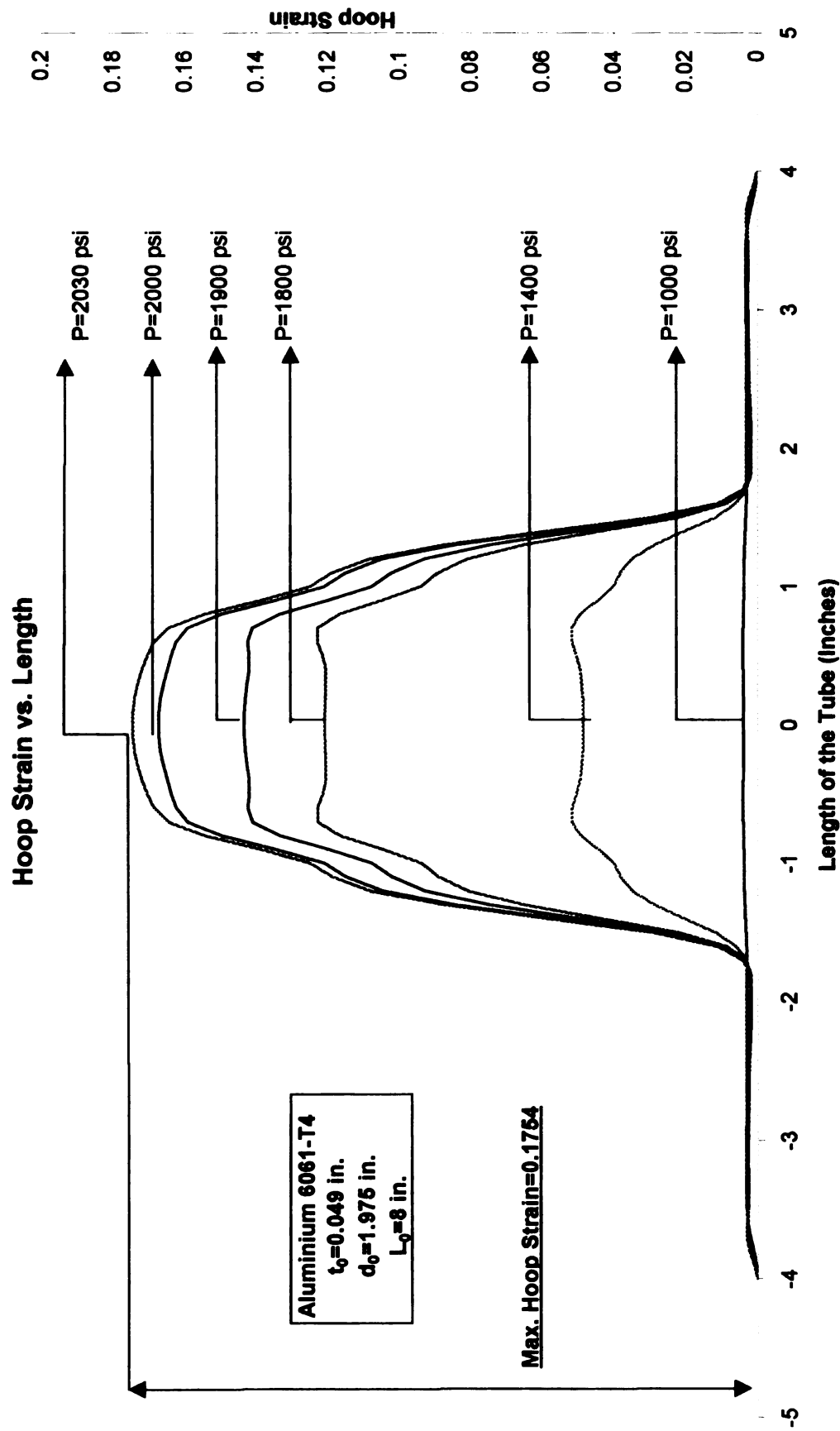


Figure 8.8 shows the intermediate shapes of a bulged steel tube at various pressure levels. Those deformed shapes were predicted by AXHD program using the displacement stroke-internal pressure history shown in figure 8.9, obtained from analytical equations given by [Asnafi, N. et al, 1999] in order to maintain a proportional axial to hoop strain ratio of  $-0.5$ . The final displacement stroke was 0.24" (6.1 mm) at the maximum pressure level of 5220 psi in the tube bulging process.

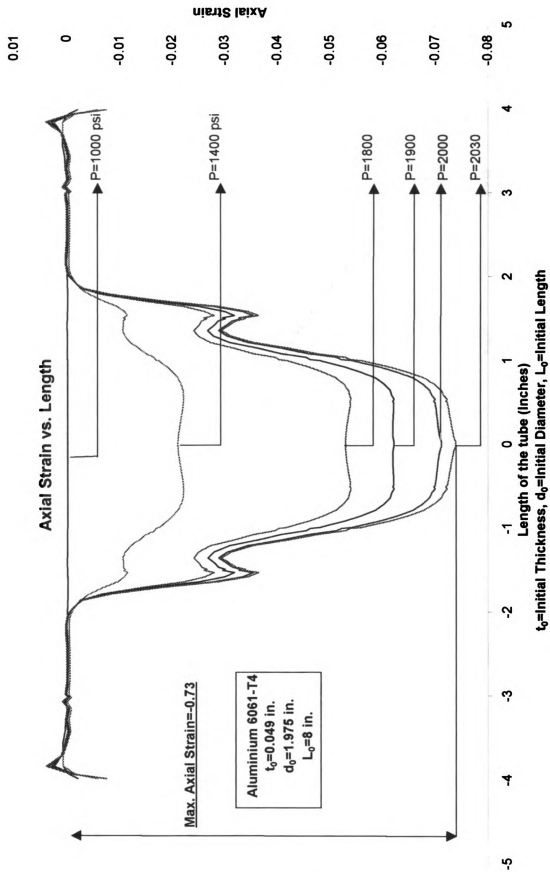
Figures 8.10 through 8.12 show the evolution of hoop strain, axial strain and the maximum thickness reduction as a function of the internal pressure. The maximum thickness strain at the maximum pressure level of 5220 psi is 15.57%. The maximum hoop and axial strains predicted by AXHD program were 28% and  $-10.9\%$ , respectively. These predicted values compared very well against measured maximum failure hoop and axial strains of 29% and  $-10\%$  reported by [Asnafi, N. et al, 1999]. Finally, figure 8.13 shows the predicted major and minor strains by AXHD program against experimentally measured [Asnafi, N. et al, 1999] and numerically predicted Forming Limit Curves (FLC) based on shear instability [Lee & Kim et al., 1989], at the maximum pressure level of 5220 psi. These results show that the steel tube is about to the fail (burst) in the middle of the tube where maximum bulge occurs.



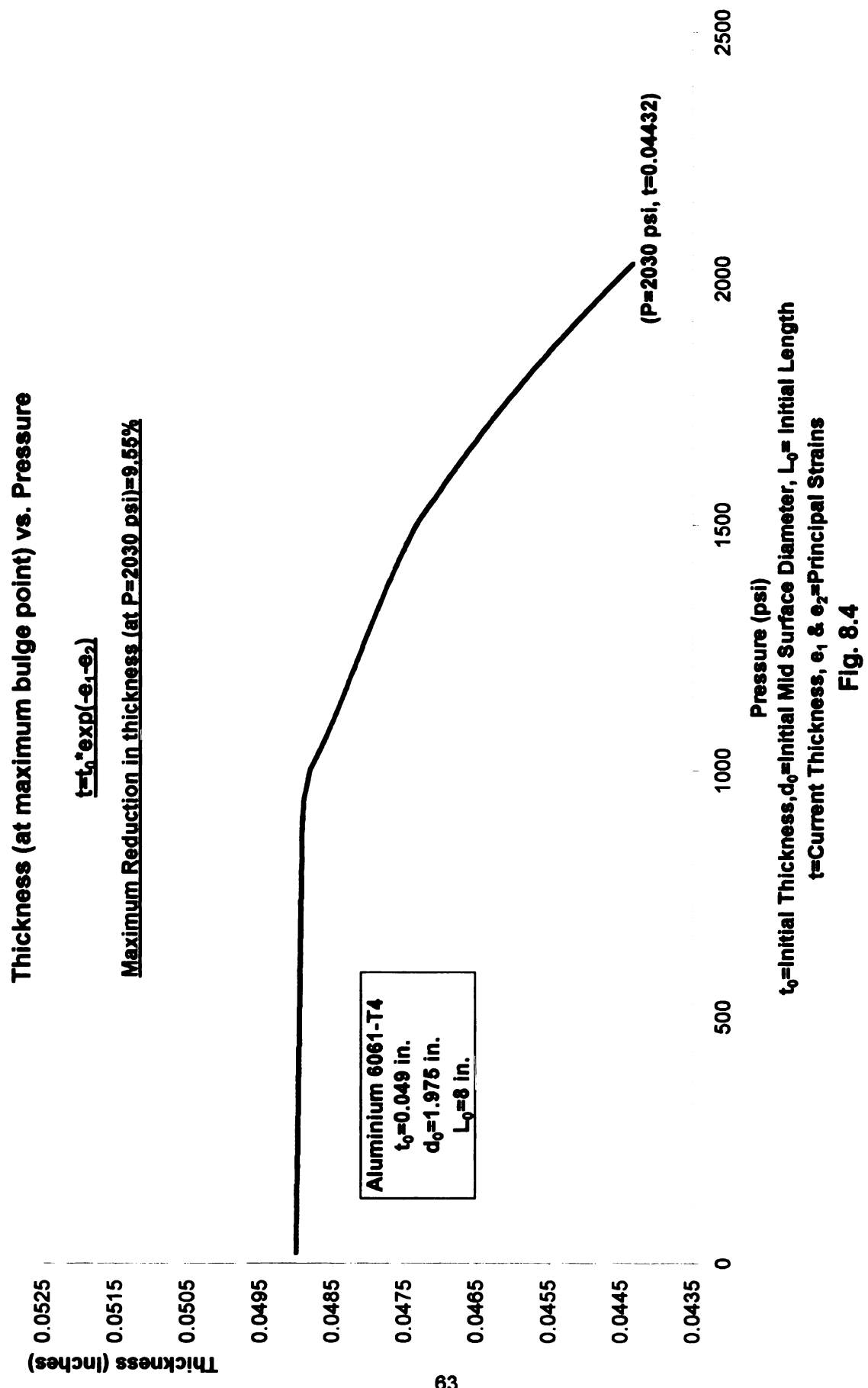
**Fig. 8.1**



**Fig. 8.2**









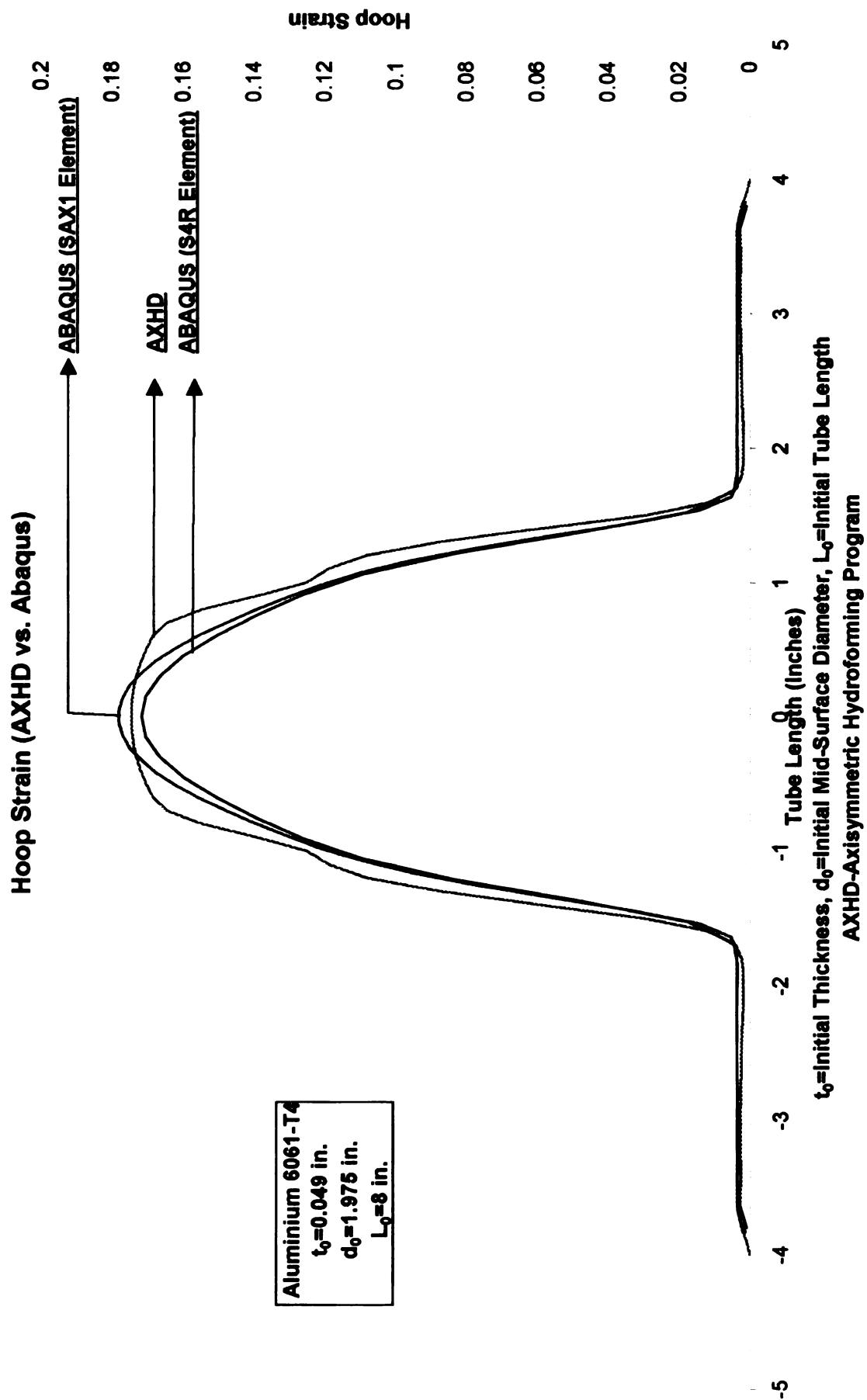
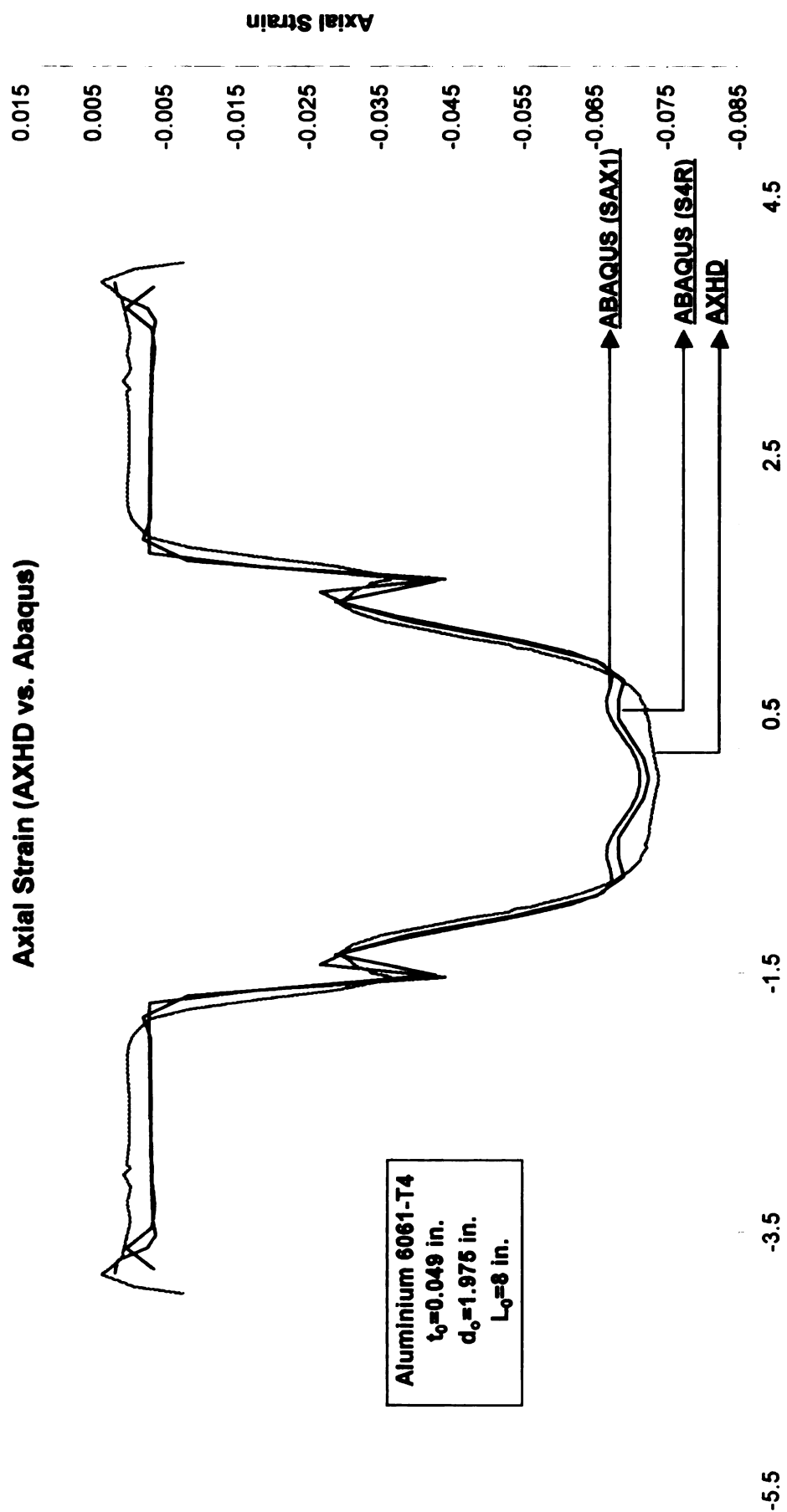
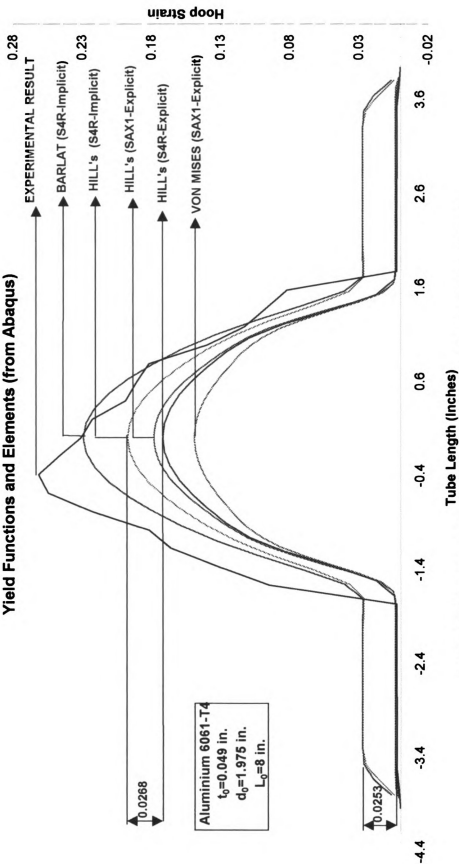


**Fig. 8.5**

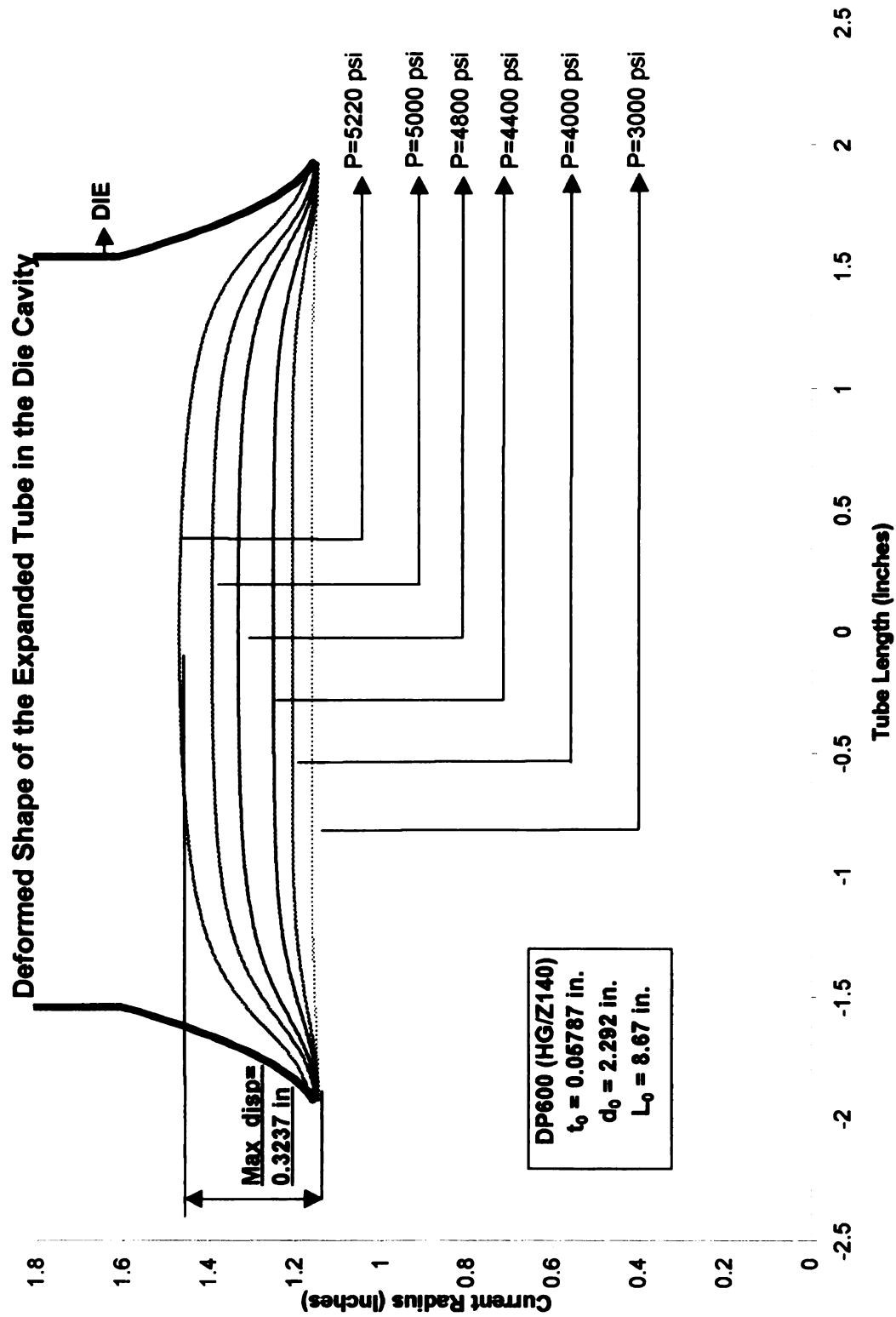




# Hoop Strain Comparison for Different Yield Functions and Elements (from Abaqus)

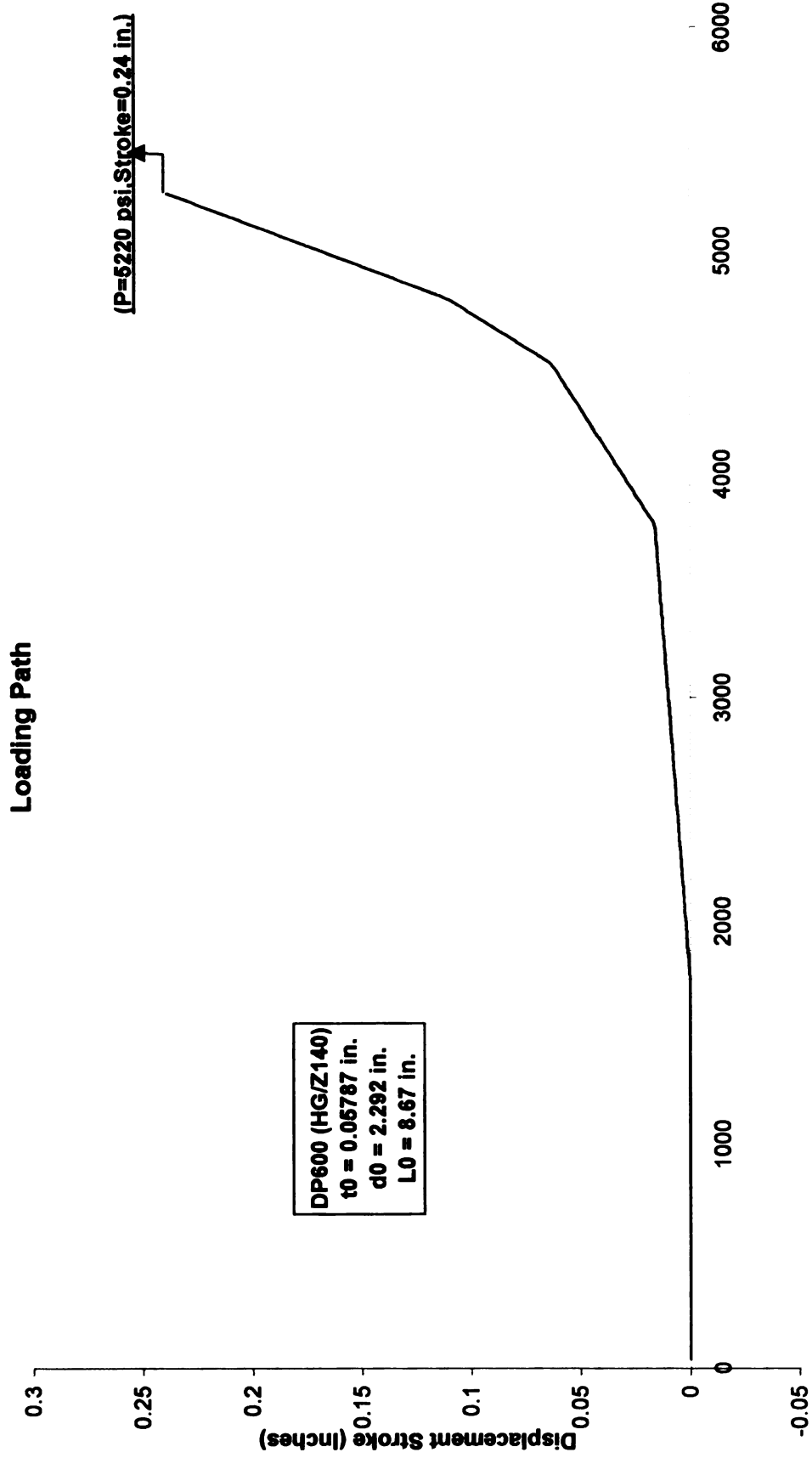


$t_0$ =Initial Thickness,  $d_0$ =Initial Mid-Surface Diameter,  $L_0$ =Initial Tube Length  
S4R-General Shell Element (reduced integration), SAX1-Axisymmetric Shell Element  
Fig. 8.7

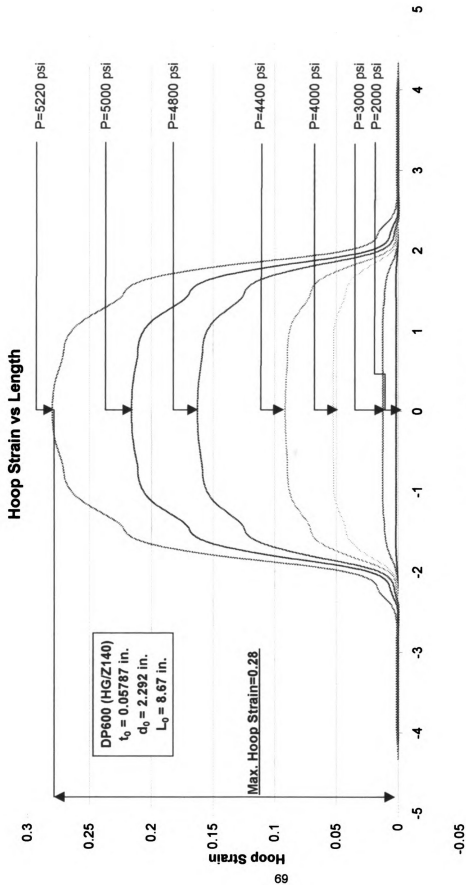


$t_0$ =Initial Thickness,  $d_0$ =Initial Diameter,  $L_0$ =Initial Tube Length

Fig. 8.8



**Pressure (psi)**  
 $t_0$ =Initial Thickness,  $d_0$ =Initial Diameter,  $L_0$ =Initial Tube Length  
**Fig. 8.9**



Length of the Tube (Inches)  
 $t_0$  = Initial Thickness,  $d_0$  = Initial Diameter,  $L_0$  = Initial Tube Length  
**Fig. 8.10**

# Axial Strain vs Length

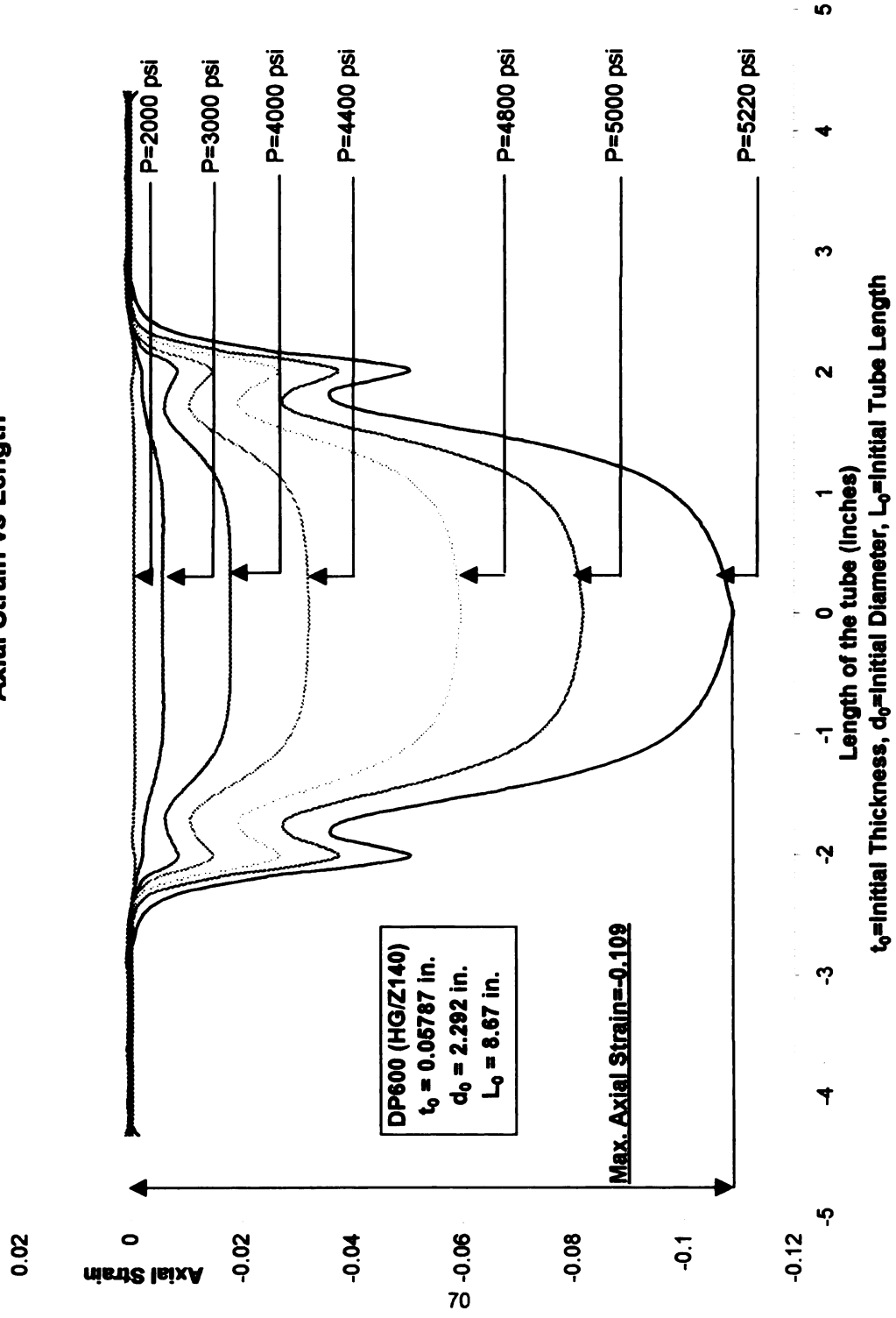
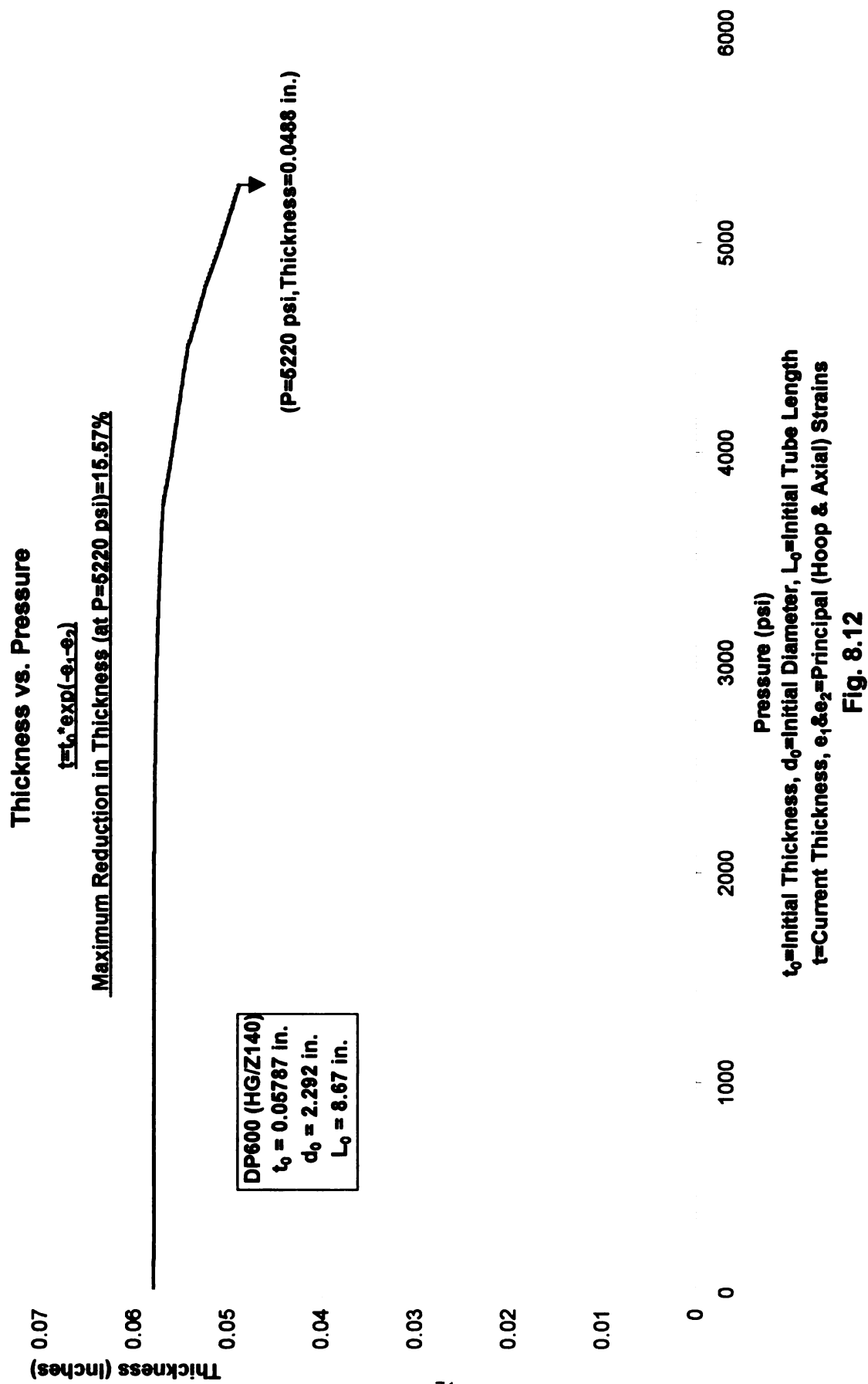
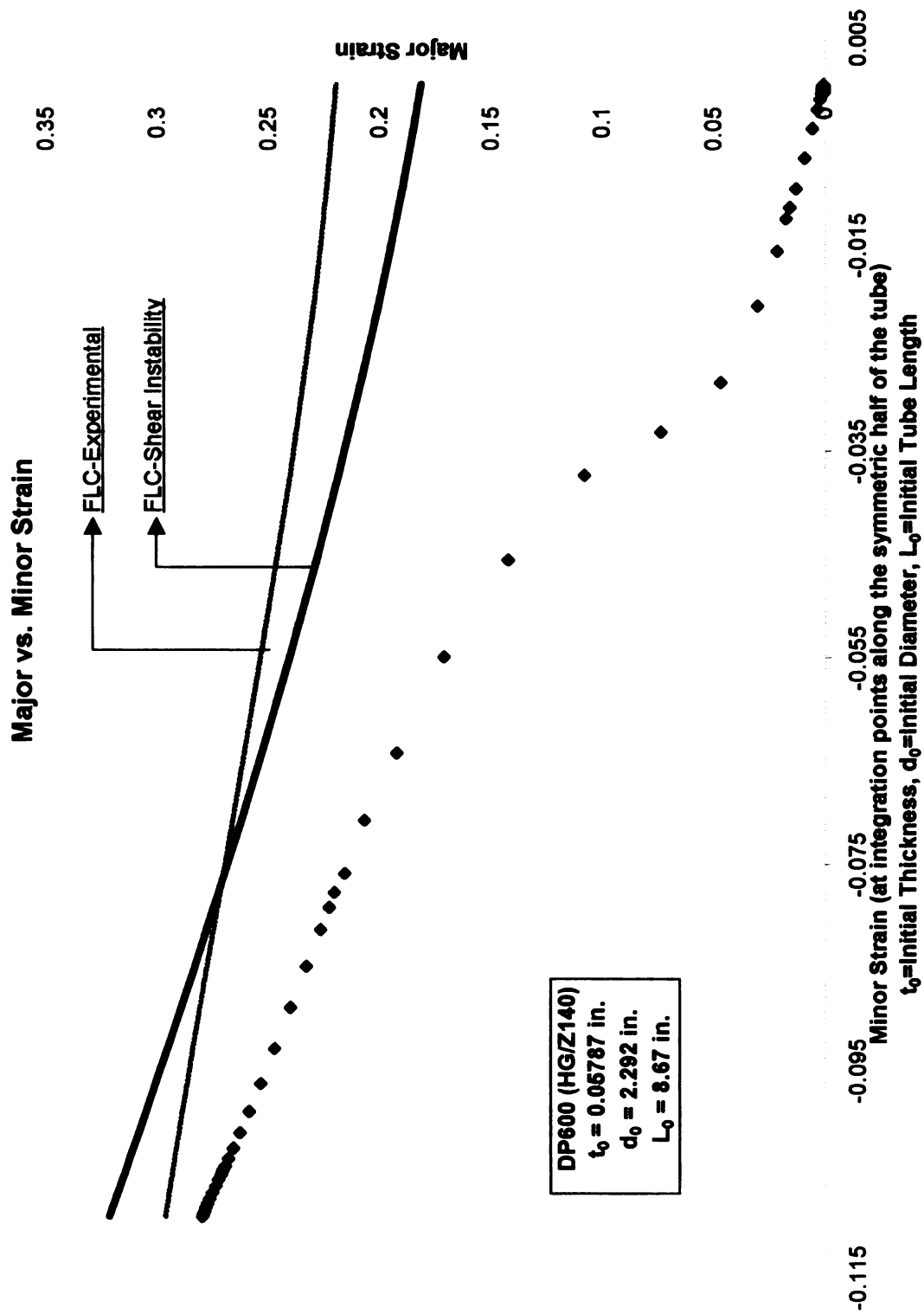


Fig. 8.11





**Fig. 8.13**



## **CHAPTER 9**

### **CONCLUSIONS**

An Axisymmetric Hydroforming finite element analysis program has been developed based on the formulations presented in the thesis. Fourier series interpolation functions, which reduce the size of global stiffness matrix and the number of variables drastically, are employed for approximating the displacements. The program is very efficient in predicting deformations for free-forming stage of tube hydroforming under simultaneous action of internal pressure and displacement stroke. Failure model based on FLD is incorporated in the code. The results from the program are compared with the results from commercial code (ABAQUS) and experimental measurements and are found to be in good agreement.

In the future, this code is to be extended for 3D analysis of tube hydroforming process. It is also planned to develop an ability to optimize the loading curve (pressure vs. stroke) for improving the material shaping abilities.

## **APPENDICES**

## APPENDIX A

According to the total Lagrangian formulation discussed in Chapter 2 (Thin shell theory), we derived the membrane strain, rotation of normal vector and the current principal centerline curvature used in Chapter 3 (Kinematics) and compared with the formulation developed by Corona and Pourboghraat (1998) and Brush and Almroth (1975).

### 1. Membrane strain

For *straight segment*, the curvature  $K_1=0$ , then from Eq.(2.15) ,

$$\lambda_1 = [(1 + u_{,s})^2 + w_{,s}^2]^{\frac{1}{2}} = [1 + u_{,s}^2 + 2u_{,s} + w_{,s}^2]^{\frac{1}{2}} \quad (1)$$

Let's approximate the square root as:

$(1 + x)^{\frac{1}{2}} \approx 1 + \frac{1}{2}x - \dots$  for  $x \ll 1$ , Eq. (1) becomes:

$$\lambda_1 \approx 1 + u_{,s} + \frac{1}{2}u_{,s}^2 + \frac{1}{2}w_{,s}^2 \quad (2)$$

Since,  $\lambda_1 = ds/dS$  and the engineering definition  $e = \frac{ds - dS}{dS} = \frac{ds}{dS} - 1 = \lambda_1 - 1$

We have the membrane strain:

$$e \approx u_{,s} + \frac{1}{2}u_{,s}^2 + \frac{1}{2}w_{,s}^2 \quad (3)$$

which is used in Chapter 3 as Eq. (3.4) and Eq. (1.6) in Brush and Almroth (1975).

### 2. Rotation of normal vector

We assumed the angle between the current normal vector  $\hat{n}$  and the  $S$  (arc length) is  $\alpha$ , the angle between the current normal vector  $\hat{n}$  and normal vector  $\hat{N}$  at the reference is  $\beta$ .

Then, we have  $\beta + \frac{\pi}{2} = \alpha$  , and  $\hat{n} \cdot \hat{A} = \cos\alpha = -\sin\beta$  (4)

Substituting Eq.(2.17) into Eq.(4), we obtain:

$$\sin\beta = \frac{d}{\lambda_1} = \frac{w_{,s} + K_1 u}{\lambda_1} = \frac{w_{,s} + K_1 u}{\sqrt{(1 + u_{,s} - K_1 w)^2 + (w_{,s} + K_1 u)^2}} \quad (5)$$

For *straight line segment* ( $K_1=0$ ), according to assumption1, Eq.(5) becomes

$$\sin\beta \approx \beta = \frac{w_{,s}}{\sqrt{(1 + u_{,s})^2 + w_{,s}^2}} \quad (6)$$

According to assumption 2 and  $w_{,s}^2 \ll 1$ , Eq. (6) becomes:  $\beta = w_{,s}$ , for the coordinates shown in Figure 3.2, we have the normal vector rotation for straight segment

$$\beta = -w_{,s} \quad (7)$$

which is used in Chapter 3 as Eq. (3.1).

### 3. The current principal centerline curvature

For *straight segment* ( $K_1=0$ ), the centerline curvature at the current configuration,  $k_s$ , will be obtained from Eq. (2.21):

$$k_s = \frac{cd_{,s} - dc_{,s}}{\lambda_1^3} = \frac{(1 + u_{,s})w_{,ss} - w_{,s}u_{,ss}}{\lambda_1^3} \quad (8)$$

According to assumption 2 ( $u_{,s} = u_{,ss} = 0$ ),  $\lambda_1 \approx \sqrt{1 + w_{,s}^2}$ , the Eq.(8) becomes:

$$k_s = \frac{w_{,ss}}{(1 + w_{,s}^2)^{\frac{3}{2}}} \quad (9)$$

which is used in Chapter 3 as Eq. (3.5).

## APPENDIX B

Here we try to prove the equivalence of two formulations in the pressure modeling, i.e.:

$$F_{Ext}^P = p \sum_{i=1}^I \int_{L_p^i} \hat{n}^i \frac{\partial(\Delta u^i)}{\partial \underline{c}} R^i dL_p^i \approx -p \sum_{i=1}^I \int_{L_p^i} \frac{\partial(\Delta w^i)}{\partial \underline{c}} R^i dL_p^i \quad (1)$$

From the Chapter 3 kinematics, for the point on mid-surface, we have

$$\xi^i = Z_0 + (s + u^i) \sin \theta - w^i \cos \theta \quad (2.a)$$

$$\eta^i = Y_0 + (s + u^i) \cos \theta + w^i \sin \theta \quad (2.b)$$

Define  $\hat{n}^i$  is the unit outward normal to the meridian segment  $L_p^i$ , then we have

$$\hat{n}^i = \frac{\left(-\frac{\partial \xi^i}{\partial s}, \frac{\partial \eta^i}{\partial s}\right)}{\left\| \left(-\frac{\partial \xi^i}{\partial s}, \frac{\partial \eta^i}{\partial s}\right) \right\|} \quad (3)$$

where

$$\frac{\partial \xi^i}{\partial s} = \left(1 + \frac{\partial u}{\partial s}\right) \sin \theta - \frac{\partial w}{\partial s} \cos \theta \quad (4.a)$$

$$\frac{\partial \eta^i}{\partial s} = \left(1 + \frac{\partial u}{\partial s}\right) \cos \theta + \frac{\partial w}{\partial s} \sin \theta \quad (4.b)$$

$$\left\| \left(-\frac{\partial \xi^i}{\partial \phi}, \frac{\partial \eta^i}{\partial \phi}\right) \right\| = \left\{ \left(1 + \frac{\partial u}{\partial s}\right)^2 + \left(\frac{\partial w}{\partial s}\right)^2 \right\}^{1/2} \approx 1 \quad (4.c)$$

We also have

$$\frac{\partial(\Delta u^i)}{\partial \underline{c}} = \left( \frac{\partial(\Delta \eta^i)}{\partial \underline{c}}, \frac{\partial(\Delta \xi^i)}{\partial \underline{c}} \right) \quad (5)$$

where

$$\Delta \xi^i = \Delta u^i \sin \theta - \Delta w^i \cos \theta \quad (6.a)$$

$$\Delta \eta^i = \Delta u^i \cos \theta + \Delta w^i \sin \theta \quad (6.b)$$

Combining (3), (4.a-c), (5) and (6.a-b), we have

$$\begin{aligned} \hat{n}^i \frac{\partial(\Delta u^i)}{\partial \tilde{c}} &= \left( -\frac{\partial(\Delta w^i)}{\partial \tilde{c}} + \frac{\partial w^i}{\partial s} \frac{\partial \Delta u^i}{\partial \tilde{c}} - \frac{\partial u^i}{\partial s} \frac{\partial \Delta w^i}{\partial \tilde{c}} \right) \\ &\approx -\frac{\partial(\Delta w^i)}{\partial \tilde{c}} \end{aligned} \quad (7)$$

Thus, we have proven Eqn. (1).

Since  $\frac{\partial^2(\Delta w^i)}{\partial^2 \tilde{c}} = 0$ , there will be no stiffness matrix due to pressure going to left side

of Newton-Raphson expression.

## REFERENCES

## REFERENCES

- Asnafi N. and Skogsgardh A., 1999, Theoretical and experimental analysis of stroke-controlled tube hydroforming, *Materials Science and Engineering A279* (2000) 95-110.
- Asnafi N., 1999, Analytical Modelling of Tube Hydroforming, *Thin-Walled Structures* 34 (1999) 295-330.
- Lee D. N. and Kim Y. K., 1989, Forming Limit Diagrams for Stainless Steel clad Aluminium Sandwich sheets, Internal Report, Seoul National University.
- Bressan J. D. and Williams J. A., *Int. J. Mech. Sci.* 25 (1983) 155.
- Ahmetoglu M. and Altan T., 2000, Tube hydroforming: state-of-the-art and future trends, *J Mater Process Tech* 98: (1) 25-33.
- Anon, 1997, Hydroforming technology, *Advanced Material Process*, 151(5) ,50-53
- Bathe, K-J, 1982, *Finite Element Procedures in Engineering Analysis*. Prentice-Hall, New Jersey.
- Becker, R.C., 1992, An efficient semi-implicit integration algorithm for anisotropic flow potentials
- Brush, D.O. and Almroth, 1975, *Buckling of Bars, Plates, and shells*, McGraw-Hill.
- Choudhry, S. and Lee, J.K., 1994, Dynamic plane-strain finite element simulation of industrial sheet metal forming processes, *Int. J. Mech. Sci.* Vol.36, No. 3, pp.189-207.
- Corona, E. and Pourboghra, F., 1998, Bending-Stretch Forming of Extrusions- BETGES Computer Program Manual, Alcoa internal report, March.
- Dohmann, F. and Hartl, Ch., 1997, Tube hydroforming: research and practical application, *J. Mater Process Tech* 71 174-186.
- Dohmann, F. and Hartl, Ch., 1996, Hydroforming: a method to manufacture light-weight parts, *J Mater Process Tech* 60 669-676.
- Flugge, W., 1973. *Stresses in Shells*, 2nd Edition. Springer-Verlag, New York.
- Germain, Y., Chung, K. and Wagoner, R.H., 1989, *Int. J. Mech. Sci.* Vol. 31, No1, pp. 1-24.
- Hibbitt, H. D., 1979, "Some follower forces and load stiffness", *Int. J. num. Mech. Engng*, 14, 937-941.



Hsu, Tze-Chi and Chu, Chan-Hung, 1995, A finite element analysis of sheet metal forming process, J Mater Process Tech 54 , 70-75.

Hu, P., Liu, Y.Q., Li, Y.X. and Lian, J., 1997, Rigid viscoplastic finite element of the gas-pressure constrained bulging of superlastic circular sheets into cone disk shape dies, Int. J. Mech. Sci. Vol. 39, No.4, pp. 487-496.

Kobayashi, S., Oh, S.I and Altan, T., 1989, Metal Forming and the Finite Element Method, Oxford University Press, New York.

Longhouse, B., 1998, Applied pressure sequence hydroforming, 3<sup>rd</sup> Annual automotive tube fabricating.

Marc's Theory and user information

Morphy, G., 1997, Hydroforming high strength steel tube for automotive structural applications using expansion, SAE International Congress & Exposition.

Nagtegaal, Joop C. and Rebelo, N., 1988, On the development of a general purpose finite element program for analysis of forming processes, Int. J. Num. Methods Eng., 25, 113-131.

Ni, C.M., 1994, Stamping and hydroforming process simulation with a 3D finite element code, SAE Paper #940753, SAE SP-1021

Noh, T.S. and Yang, D.Y., 1998, A general formulation for hydroforming of arbitrarily shaped boxes and its application to hydroforming of an elliptic-circular box, Journal of Manufacturing Science and Engineering, August, Vol. 120 481-488.

Oden, J.T. and Pires, E.B., 1983, Nonlocal and nonlinear friction laws and variational principles for contact problems in elasticity, ASME J. Appl. Mechs., Vol. 50, 67-76.

Oh, S.I., 1982, Finite element analysis of metal forming processes with arbitrarily shaped dies, Int. J. Mech. Sci. Vol. 24, No. 8, pp. 479-493.

Pourboghrat, F., Karabin, M.E., Becker, R.C. and Chung, Kwansoo, 2000, "A hybrid membrane/shell method for calculating springback of anisotropic sheet metals undergoing axisymmetric loading", International Journal of Plasticity 16 677-700.

Sheet-S, Ohio State University

Siebert K., Haussermann M. and Losch B., et al, 2000, Recent developments in hydroforming technology, J Mater Process Tech 98: (2) 251-258.

The ABCs of Hydroforming, Vari-Form Inc.

Wang, N.M. and Tang, S.C., 1988, Analysis of bending effects in sheet forming operations, *Int. J. Num. Methods Eng.*, 25 253-267.

Wang, N.M. and Budiansky, B., 1978, Analysis of sheet metal stamping by a finite element method, *ASME J. Appl. Mechs.*, Vol. 45 73-82.

Zhang, SH, 1999, Developments in hydroforming, *J Mater Process Tech* 91:(1-3) 236-244.

MICHIGAN STATE UNIVERSITY LIBRARIES



3 1293 02455 3335